2D PEROVSKITE NANOSHEETS FOR MULTIFUNCTIONAL DEVICE FABRICATION AND BIOLOGICAL APPLICATIONS

BENSU GÜNAY

Master's Thesis

Graduate School
Izmir University of Economics
Izmir
2021

2D PEROVSKITE NANOSHEETS FOR MULTIFUNCTIONAL DEVICE FABRICATION AND BIOLOGICAL APPLICATIONS

BENSU GÜNAY

A Thesis Submitted to

The Graduate School of Izmir University of Economics

Master of Science Program in Bioengineering

Izmir

2021

ABSTRACT

2D PEROVSKITE NANOSHEETS FOR MULTIFUNCTIONAL DEVICE FABRICATION AND BIOLOGICAL APPLICATIONS

Günay, Bensu

Master of Science Program in Bioengineering

Advisor: Asst. Prof. Dr. Özge Sağlam

Co-Advisor: Assoc. Prof. Dr. Zeynep Fırtına Karagonlar

June, 2021

The main purposes of the thesis are the fabrication of a multifunctional device structured by upconverting nanosheets and the investigation of the biocompatibility of the two-dimensional nanosheets for biological applications. The layered perovskites $K_2Ln_2Ti_3O_{10}$ were synthesized in different stoichiometric ratios co-doped with Tm^{3+}/Er^{3+} ions to obtain red emission via the upconversion process. The 2.5% Tm^{3+}-20% Er^{3+} co-doped layered material was obtained with lateral size within the range of 300 nm to 2.5 μm. The thickness of nanosheets was determined around 2-3 nm showing the single nanosheets successfully were obtained. Upconversion properties of the Tm^{3+}/Yb^{3+} and Er^{3+}/Yb^{3+} co-doped nanosheets structured films prepared with 20 sequences of layer-by-layer technique showed the blue emission due to the $^1G_4 \rightarrow {}^3H_6$

transition and green emission due to the $^4S_{3/2} \rightarrow {}^4I_{15/2}$ and $^2H_{11/2} \rightarrow {}^4I_{15/2}$ transitions, respectively. On the other hand, Tm^{3+}/Er^{3+} co-doped nanosheets structured films exhibited red and green emission via the upconversion process. In the case of Er^{3+}/Yb^{3+} co-doped nanosheets' deposited films, the two-photon processes were involved in the green and red upconversion emissions. The films fabricated with 60 layers were also prepared using three different nanosheets. The combination of nanosheets in the film preparation displayed a white emission due to the CIE Diagram. Moreover, the cytotoxicity of nanosheets was analyzed using HepG2 and HEK 293 cell lines. While the toxicity of the Tm^{3+}/Er^{3+} co-doped layered material for the HEK 293 cell line was 45.7%, the toxicity of nanosheets was 73.6%.

Keywords: Upconversion Luminescent materials, layer-by-layer assembly, nanofilm coating, 2D perovskite nanosheets, Cytotoxicity Assay

ÖZET

2B PEROVSKİT NANO LEVHALARIN ÇOK FONKSİYONLU AYGIT FABRİKASYONUNDA KULLANIMI VE BİYOLOJİK UYGULAMALARI

Günay, Bensu

Biyomühendislik Yüksek Lisans Programı

Tez Danışmanı: Dr. Öğr. Üyesi Özge Sağlam

İkinci Tez Danışmanı: Doç. Dr. Zeynep Fırtına Karagonlar

Haziran, 2021

Bu tezin amaçları, frekans yükseltme özelliğine sahip nanolevhalar kullanılarak yapılandırılmış çok işlevli bir cihaz tasarımı ve biyolojik uygulamalar için iki boyutlu nanolevhaların biyouyumluluğunun araştırılmasıdır. $K_2Ln_2Ti_3O_{10}$ yapıda katmanlı perovskitler frekans yükseltme ile kırmızı ışıma elde edebilmek için farklı sitokiyometrik oranlarda Tm^{3+}/Er^{3+} iyonları ile katkılandırılarak sentezlenmiştir. 2.5% Tm^{3+}-20% Er^{3+} ile katkılı katmanlı malzemenin yanal boyutu 300 nm ile 2.5 µm arasında elde edilmiştir. Nanolevhaların kalınlığı 2-3 nm arasında belirlenmiştir ve tek nanolevhaların başarılı bir şekilde elde edildiği gösterilmiştir. Frekans yükseltme özelliğine sahip Tm^{3+}/Yb^{3+} ve Er^{3+}/Yb^{3+} ile katkılı nanolevhalar katman-katman

tekniği ile 20 kez kaplanmıştır ve hazırlanan filmler sırasıyla $^1G_4 \rightarrow {}^3H_6$ geçişi ile mavi ışıma ve $^4S_{3/2} \rightarrow {}^4I_{15/2}$ ve $^2H_{11/2} \rightarrow {}^4I_{15/2}$ geçişleri ile yeşil ışımalar göstermiştir. Öte yandan, Tm^{3+}/Er^{3+} ortak katkılı nanolevha yapılı filmler, frekans yükseltme işlemi sırasında kırmızı ve yeşil emisyon sergilemiştir. Er^{3+}/Yb^{3+} ortak katkılı nanolevhaların biriktirilmiş filmleri durumunda, yeşil ve kırmızı frekans yükseltme emisyonlarında iki foton süreçleri yer almıştır. 60 katman ile üretilen filmler ayrıca üç farklı nanolevhalar kullanılarak hazırlanmıştır. Film oluştururken nanolevhaların kombinasyonu CIE diagramında beyaz emisyon sergilemiştir. Ayrıca nanolevhaların sitotoksisitesi HepG2 ve HEK 293 hücre hatları kullanılarak analiz edilmiştir. HEK 293 hücre hattı için Tm^{3+}/Er^{3+} katkılı katmanlı malzemenin toksisitesi %45,7 iken, nanolevhaların toksisitesi %73,6 olarak belirlenmiştir.

Anahtar Kelimeler: Frekans yükseltici ışıma yapan malzemeler, katman-katman kaplama yöntemi, nanofilm kaplama, 2B perovskite nanolevhalar, Sitotokisite analizi

To my Family for their invaluable support…

ACKNOWLEDGEMENTS

First of all, I would like to express my deepest gratitude and respect to my advisor Asst. Prof. Özge Sağlam, who has impressed me the most and has encouraged me throughout my research with her patience and knowledge. She always has inspired me to be a good researcher and at the same time always kept my hope and motivation high. She has given me countless experiences in the laboratory with the doors wide open.

Secondly, I would like to express my sincere thanks to Assoc. Prof. Zeynep Fırtına Karagonlar and Assoc. Prof. Uğur Ünal for their contributions and development of my thesis.

My sincere thanks to the Scientific and Technological Council of Turkey (TUBITAK) for award-winning support 2211-National Graduate Scholarship Program (2210-C National MSc Program in the Priority Fields in Science and Technology) and financial supports (Grant number; 117M512 and 218M517). Besides that, I would like to thank Koç University Surface Science Center (KUYTAM) and the Research and Application Center for Quantum Technologies (RACQUT).

I would also like to thank my lab-mate and sister Hilal Döğer for her endless support. In addition, I would like to thank to Caner Erdoğdu, Özge Süer, Barış Dal, Hazal Gül, Sıla Köse, Sude Uyulgan, Latif Tibet Aktaş, Burçin Dersu Açıkgöz, Mehmet Faruk Cengiz, Nesrin Tezduyan and many others I did not mention, for their always amazing friendships and being motivation source in difficult situations.

Special thanks to Nur Deniz Bingül, Esra Ersöz, Beyza Emre, Ece Sarıyar, Borja López Santos, Dimitris Mitrogiannis, Paulina Mlynarczyk and Sheila Lata for their valuable insight and never-ending help.

The family is the one who knows the person best, picks them up when they fall, and shares their love all the time. I would like to express my endless love and thanks to my dear family who are the biggest support. Especially the youngest member of my family, Deniz Günay.

TABLE OF CONTENTS

LIST OF TABLES

LIST OF FIGURES

LIST OF EQUATIONS

CHAPTER 1: INTRODUCTION

Two-dimensional (2D) materials are being developed as an alternative to silicon-based technologies. The studies on 2D materials have become significant with the graphene isolation (or 2D graphite) in 2004 (Geim, 2012). 2D oxide nanosheets researched in this context are produced from oxide layered materials. Layered materials have gained different features related to their transformation from 3D to 2D when oxidized and combined with other composites. Unlike graphene, inorganic oxide layered materials are composed in the form of 2D nanosheets by chemical exfoliation besides mechanical exfoliation. 2D nanomaterials are used in nanotechnological studies due to their morphological structures and functionality, especially dielectric, magnetic, optical, superconducting, and photocatalytic applications (Zhu et al., 2018). Two dimensional (2D) nanomaterials have a place of importance for some applications in electrochemistry such as; clean energy generation and storage applications, electrochemical sensor applications, dye-sensitized solar cells, supercapacitors, batteries, fuel cells, an electrocatalyst for hydrogen evolution reaction, etc. (Thanh et al., 2018). Besides that, upconverted nanomaterials are very attractive for multifunctional applications that involve a wide range of biomedical and photonics studies (Tsang et al., 2015). The thickness of the oxide nanosheets can modify from 1 nm to a few nanometers, and their lateral sizes can reach up to 10 μm. In general, oxide nanosheets are produced from layered structures containing transition metals (Ti, Mn, Ru, Ta, Nb, Ta, W).

Titanium oxide nanosheets can demonstrate photocatalytic, dielectric, and ferromagnetic properties. In $MnO_2^{0.4-}$ nanosheets, an increase in the optical absorption of the nanosheet is observed related to the reaction of oxidation-reduction (redox) between Mn^{3+} and Mn^{4+}, which makes them usable in energy conversion/storage devices (Sun et al., 2013). $RuO_{2.1}{}^{x-}$ from the ruthenium oxide family, shows redox activity (Sugimoto et al., 2006), while $Ru_{0.95}O_2^{0.2-}$ is metallic and is used as a 2D conductor (Wang et al., 2014).

Perovskite oxide nanosheets make up the widest part of the oxide nanosheet family. These nanosheets can exhibit photocatalytic and visible radiation due to their easily interchangeable composition and their doping ability with lanthanides. The host

structure of the perovskites can be doped with various combinations of the lanthanides. According to the type of doping and its concentration, these nanosheets show luminescence properties at different wavelengths in the visible region. Ida et al. reported that $Gd_{1.4}Eu_{0.6}Ti_3O_{10}^{2-}$ nanosheets under UV light showed red luminescence as compared with the bulk form(Ida et al., 2008).

The ion-exchange ability of layered perovskites can also affect the physical, catalytic, and luminescence properties of crystal structures (Toda et al., 1996). Furthermore, lanthanide co-doped nanomaterials act as luminescent materials, and their upconversion properties can be used for multiphoton processes. Energy transfer of lanthanide co-doped nanomaterials takes place in a system where absorption and emission do not occur in the same way. Interactions between ions play a key role in the up-and downconversion luminescence of nanomaterials. When the A sites of the perovskites are doped by trivalent lanthanide ions, the oxide materials can become luminescent materials. Lanthanide-doped nanoparticles can be excited by using NIR lasers that emit strong visible/NIR light for an efficient upconversion process (Kim et al., 2009)

Ding et al. reported loading of Cr_2O_3 on the TiO_2 based titanate nanosheets (TNSs) can be used for photocatalytic activity under visible light because of their wide surface area. That feature could be advantageous for metal ions spreading and dispersing in the area (Ding et al., 2017).

Upconversion is a phenomenon that indicates one or more low-energy photons are absorbed by a material and re-radiated as higher-energy photons (Zhou et al., 2015). Materials that can cause this effect are called upconverter materials. Upconversion was discovered in the 1960s (Ovsyakin and Feofilov, 1966), and since then, especially from the infrared to the visible region, has been the focus of much research. So far Yb^{3+} / Er^{3+} (green), Yb^{3+} / Tm^{3+} (blue) and Tm^{3+}/ Er^{3+} (red) co-doped oxides, fluorides, chlorides and bromides have changed frequency magnification of host crystals (Meruga et al., 2014). Upconversion luminescence (UCL) materials can be stimulated due to high energy sources, temperature, pH, X-ray, electrical and magnetic fields, etc. from NIR excitation to the UC emission. Specifically, $Er^{3+}$and Tm^{3+} ions are affected by stimuli of temperature, and electron beams. Coherent scattering, Compton scattering, and the photoelectric effect are the most important

processes for nanomaterials' X-ray interactions (Tsang et al., 2015). Vendruscolo et al. (2020) reported Yb^{3+}/Er^{3+} co-doped $KCa_2Nb_3O_{10}$ have changeable UC properties due to using different doping ratios. In this study, four different emission bands were observed which the red (650-675 nm) region ($^4F_{9/2}\rightarrow{}^4I_{15/2}$), green (510-560 nm) ($^2H_{11/2}\rightarrow{}^4I_{15/2}$; $^4S_{3/2}\rightarrow{}^4I_{15/2}$), and violet (410-415 nm) region ($^2H_{9/2}\rightarrow{}^4I_{15/2}$) (Vendruscolo et al., 2020).

Er^{3+} doped $NaNbO_3$ nanorod perovskites had UC property with the intense green emission and weak red emission reported by Ge et al, (2016). The maximum intensity was observed at 0.5 wt% Er^{3+} doping $NaNbO_3$. The red emission had a peak at 661 nm and the intense green emission was excited from the excited state (ESA) to the ground state (GSA) at 524 and 543 nm (Ge et al., 2016).

Nanotechnology studies have become gradually important in the field of biomedicine and these studies lead to the development of nanobiotechnology (Ramos et al., 2017). Nanoscale particles (1-100 nm) show some properties that are invisible on a macroscopic scale (Urie et al., 2018). Metal-based nanomaterials, carbon allotrope, or ceramic NPs(nanoparticles) have remarkable applications in nanobiotechnology, especially in diagnosis, drug delivery systems, prostheses, and implants(Ramos et al., 2017; Urie et al., 2018). Nanomaterials are well integrated into biomedical devices because many biological systems have micro-nano scale dimensions (Ramos et al., 2017). Studies on nanomaterials aspects have gained importance in some fields such as cell imaging, drug delivery, and tumor therapy. Thus, nanomaterial-based treatments in the biomedical field are becoming widespread. In addition, the field of nanotoxicology (the science that focuses on elucidating the toxic effects of nanomaterials) is of great interest for the advancement of nanotherapeutics. Among the easily synthesized nanomaterials, the graphite (sp^2) carbon family (carbon nanotubes, graphene, graphene oxide, etc.) are frequently studied because of their physical, morphological, thermal, and electrical conductivity. Nonetheless, the biological applications of layered perovskites can light the missing points for nanobiotechnology applications.

In this thesis, upconverted nanofilms using 2D nanosheets were investigated for multifunctional device fabrication. 2D nanosheets were also analyzed for the compatibility of biological applications. Despite the lanthanide-doped perovskite

nanosheets with many varieties having already been studied. During the thesis studies, we reported the Tm^{3+}-Er^{3+} co-doped $K_2La_2Ti_3O_{10}$ (K-LTO) synthesis studies, Tm^{3+}-Er^{3+} co-doped upconverting nanosheets, and their toxicity to the literature (Gunay et al., 2021). The synthesis of 2.5%Er^{3+}-5%Yb^{3+}, and 2.5%Tm^{3+}-20%Yb^{3+} co-doped K-LTO were directly performed as reported by Sağlam, (2020). Based on Ruddlesden-Popper Type K-LTO material, erbium (Er^{3+}), ytterbium (Yb^{3+}), and thulium (Tm^{3+}) from the lanthanide groups were synthesized in different stoichiometric ratios and doped proportionally with the lanthanum (La^{3+}) element. 2D nanosheets were obtained from these newly co-doped K-LTO layered perovskites. Subsequently, nanofilm formation was achieved by combining nanosheets layer-by-layer assembly. Er^{3+}-Yb^{3+}, Tm^{3+}-Yb^{3+}, and Tm^{3+}-Er^{3+} co-doped nanosheets were coated because of their upconversion behavior of the green, blue and red regions, respectively. These green, blue and red emissions refer to RGB reflections for the optical devices and this device was planned to be designed in nanoscale. X-Ray Diffractometer, Atomic Force Microscopy, Scanning Electron Microscopy-EDX, UV/Vis/NIR spectrometer, upconversion measurements were performed for the characterization of layered powders, protonated forms, 2D nanosheets, and nanofilm coatings. The effect of nanosheets on cell viability was investigated for the determination of biocompatibility to the body. Moreover, the usability of nanosheets in optical-based biomedical fields was aimed to be brought to the literature. This thesis has been an interdisciplinary study that brings together the subjects of physics, chemistry, biology, and materials science.

CHAPTER 2: LITERATURE REVIEW

2.1 Layered Perovskites

Perovskites having a chemical formulation of ABX_3, are crystal structures formed by strong interactions between two cations and one anion (Assirey, 2019). A is a cation of alkali earth metals or lanthanides and B is a cation of transition metal ions. The octahedron form of X ions surrounds B cations (Atta et al., 2016). X can be oxygen anion or other big ions (halides, sulfides, nitrides, etc.) (Assirey, 2019). Perovskite materials contain different characteristic oxides combinations with the formula ABO_3 (stoichiometric ratio 1:1:3) such as; WO_3, $NaTaO_3$, $SrTiO_3$, $BaTiO_3$ which have insulating, ReO_3, $KMoO_3$, $LTiO_3$ having a metallic and $PbCrO_3$, $CaMnO_3$, $LaFeO_3$ having magnetic properties. (Bhalla et al., 2000; Atta et al., 2016).

The ideal cubic perovskite units were described by Hines et al. with the interaction between BO_6 octahedral forms and "A" cations (Hines et al., 1996). "A" cations have a bigger size than the B cations in the ABO_3 ideal structure for all perovskite forms (Ono et al., 2017). The ideal octahedral cubic forms stabilize between atoms with the 12-fold coordination of A side cations and the 6-fold coordination of B cations (Atta et al., 2016) The ABO_3 ideal cubic perovskites and their parts are shown in Figure 1.

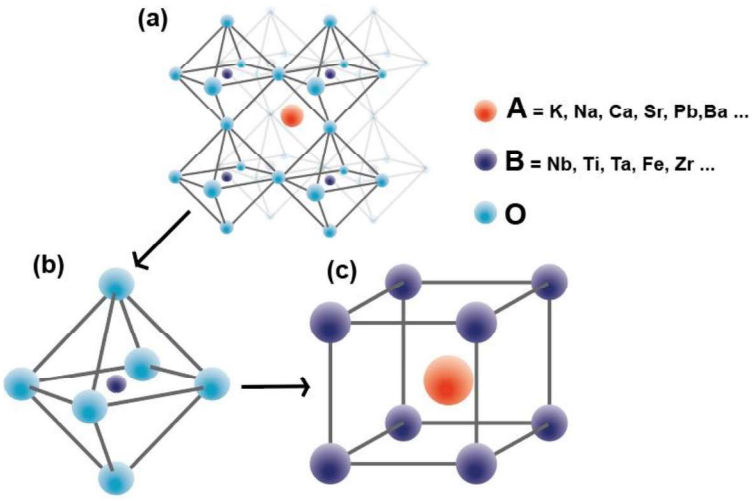

Figure 1. ABO_3 ideal cubic perovskite schematic(a), BO_6 octahedral units (b), A and B cations stabile interactions in perovskites(c) (Source: Hines, Allan and Flavell, 1996; Assirey, 2019)

r_A, r_B and r_O represent the radius of A cation, B cation, and O anion, respectively. If the Goldschmidt's tolerance factor, which understanding suitability of perovskites is between 0.77 and 1.05, the perovskites are in "ideal" cubic form. In detail, $1.00 < t < 1.13$ shows hexagonal, $0.9 < t < 1.0$ shows cubic and $0.75 < t < 0.9$ shows orthorhombic form of perovskite structures (Atta, Galal and El-Ads, 2016). The distortion is related to crystal stability. If the $t > 1$ shows that the perovskite materials exhibit high ferroelectric or dielectric properties and the last option $t < 1$ shows asymmetry and non-stabilized form of perovskites (Galasso, 1969; Tidrow, 2014).

Generally, electron localization and energy band states can change due to the type of perovskites (Szuromi and Grocholski, 2017). Related to configuration, there are such different perovskite structures. Layered perovskite (A_2BO_4), perovskite (ABO_3), triple perovskite ($A_2A'B_2B'O_9$), and double perovskite($A_2BB'O_6$) are some examples of perovskite structures (Assirey, 2019). According to its structure, composition, physical and chemical attractions, perovskites possess many properties, including dielectricity, ferroelectricity, piezoelectricity, multiferroicity, superconductivity, colossal magnetoresistance (CMR), catalytic activity, and optical properties (Assirey, 2019; Osada and Sasaki, 2018).

Layered perovskites can be classified into three groups is called Dion-Jacobson $A'[A_{m-1}B_mO_{3m+1}]$, Ruddlesden-Popper $A'_2[A_{m-1}B_mO_{3m+1}]$, and Aurivillius $[Bi_2O_2][A_{m-1}B_mO_{3m+1}]$. (A′ = alkali metals, A = alkali earth metals; B = transition metals and m = thickness between perovskite layers). Ruddlesden-Popper phases as a host material are twice that of layer charge than the Dion-Jacobson phases for intercalation (Tahara et al., 2007). The types of layered perovskites are shown in Figure 2.

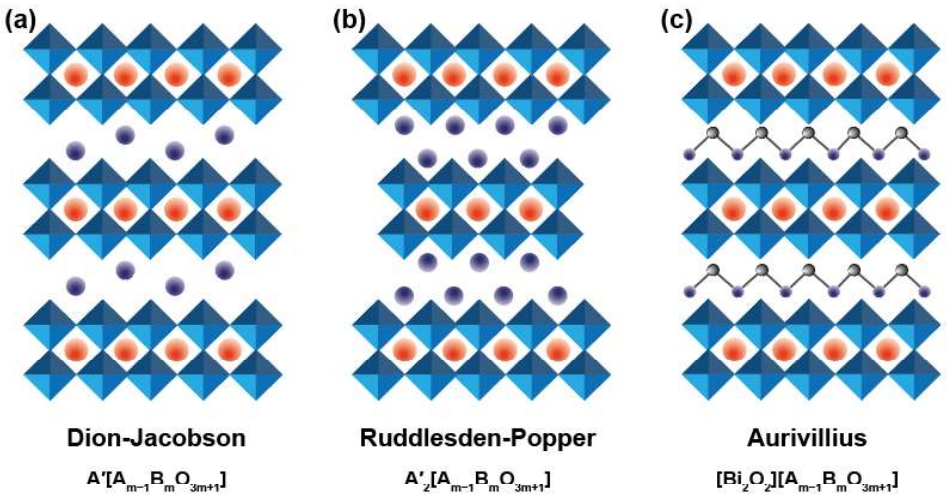

Figure 2. (a) Dion-Jacobson, (b) Ruddlesden-Popper and (c) Aurivillius types of layered perovskites (Source: Khodabakhsh, 2018)

A can be alkali metal cations (Li, Na, K, Rb), A' can be rare earth metals (La, Tm, Er, Yb, Gd, Eu, Nd, Sm, Dy) and m represents the number of BO_6 units for the type of perovskites. B can be transition metals that are in the center of the BO_6 units. Besides, RP-type perovskites are formed as a triple layer. Oxide forms of layered perovskites have an ion-exchangeable property and their BO_6 octahedral units can be NbO_6, TiO_6, and TaO_6 (Toda et al., 1996). Layered oxides can be affected by the ion exchange in the hydrous phase because water ions can intercalate into the oxide layers. The moisture can be affected by the layered powder perovskites.

Rodionov et al., (2019) reported that $K_2Nd_2Ti_3O_{10}$ layered oxide showed a hydrated form ($K_2Nd_2Ti_3O_{10} \times H_2O$) because of the atmospheric humidity. After the powder layered material was kept in 75% humid air, an increase in distance was observed. When the water ions intercalate into the layers, distance can increase between the layers.

The advantages of ion-exchange, layered perovskites can have the ability of catalytical (Allen et al., 2010; Domen et al., 1993), ion conductivity (Schaak and Mallouk, 2002), up- down- conversion as a luminescence (Uppuluri et al., 2018). Besides, 2D layered RP nanomaterials possess higher environmental stability and impressive optoelectronic properties in comparison with 3D RP nanomaterials(Pan et

al., 2020). In this thesis RP-type perovskites were used because they can be coped with lanthanide ions and their lateral sizes are approximately micrometer after the exfoliation. Thus, the substrate can be easily covered with large lateral size and this can prevent leakage current problems for the device fabrication.

2.2. Two Dimensional Perovskites

The "nanosheets" term was defined by Sasaki et. al in 1996 after finding 2D titanium oxide exfoliation (Sasaki et al., 1996). Conversion of 2D nanosheets can be produced with mechanical splitting, chemical vapor deposition (CVD), exfoliation in liquid with mechanical forces, other chemical interactions in water, ion intercalation/exchange, etching, and oxidation in specific areas. Up to now, graphene, graphene oxide (GO), reduced graphene oxide (RGO), transition metal dichalcogenides (TMDs), layered double hydroxides (LDHs), hexagonal boron nitride (h-BN), and transition metal -carbides, carbonitrides, nitrides- (MXenes) have been studied in an extensive area with their 2D nanosheet form (Fu et al., 2018). The exfoliation process, which is called the delamination of layered materials, takes place by exchanging ions in the interlayer, and layered perovskites, titanium oxides, and manganese oxides can be successfully converted into 2D using this method. These materials exfoliate layers as nanosheets when solvents with large molecules react with hydrogen atoms in the intermediate layer after the protonation process (Osada and Sasaki, 2009).

Table 1. 2D nanosheets building blocks for nanofilm fabrication (Source: Azadmanjiri et al., 2016)

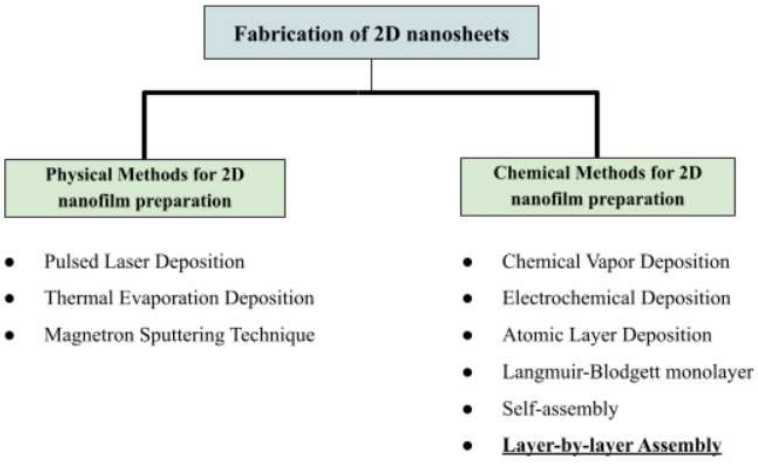

The oxide nanolayers for nanofilm coating can be obtained as negatively charged crystallites dispersed in a colloidal suspension, allowing the nanolayers to be coated by the layer-by-layer assembly. A variety of different nanostructured films or devices can be arranged at the nanoscale by the layer-by-layer assembly. The negatively charged nanosheets are deposited layer by layer by electrostatic forces using oppositely charged polyelectrolytes such as poly (diallyl dimethylammonium chloride) (PDDA) and poly(ethyleneimine) (PEI) (Osada and Sasaki, 2012)

The substrate, which is immersed in the nanosheet solution and kept for some minutes, is cleaned from the deposits on the surface with ultra-pure water. After that, it is kept in the polycation solution for some minutes and the surface is made positively charged. Again, the residues accumulated on the substrate are removed with water and immersed in the negatively charged nanosheet solution. Thus, the layer-by-layer coating is achieved due to positive and negative charged interactions (Sasaki et al. 2001). In addition, nanosheets, which are used as building blocks in nanofilm production, can be combined with metal complexes, ions, and materials that are difficult to combine with the existing beam epitaxy. Thus, it is possible to produce hybrid materials formed by combining inorganic nanosheets, develop superlattice-type structures, and construct devices from nanosheets. Nanofilms consisting of nanosheets are produced by layer-by-layer and flocculation methods with beaker epitaxy. In particular, the layer-by-layer method of electrostatic sequential adsorption is very effective for this purpose. It is possible to produce nanometer-thick composite films using the layer-by-layer method. This wet chemistry approach, also called 'beaker epitaxy' with inorganic nanosheets, is methodologically very simple, inexpensive, and environmentally friendly when compared to beam epitaxy, and provides researchers with the opportunity to work at the atomic level (L. Wang et al., 2019; Wang et al., 2019). In this thesis layer-by-layer assembly was performed for the film fabrication using 2D nanosheets. In response to the infrared light that the RP-type nanosheets are exposed to, it is aimed to emit green, blue, and red in the visible region according to co-doped with lanthanide ions.

2.3. Upconversion in Luminescent Materials

Luminescence is the spontaneous emission and absorption of photons due to electrons' excitation. There are various luminescence types related to modes of excitation. If the emission occurs with light that is called photoluminescence, the emission occurs with an electrical field that is called electroluminescence or by chemical attractions that are called chemiluminescence, similarly (Bergman and McHale, 2011). Photoluminescence has an important area for science and technology, especially fundamental science (physics, chemistry, and biology), materials science, and medicine(Valeur and Berberan-Santos, 2011). Fluorescence microscopy, optical brighteners, plasma screen, phosphorous paints, safety inks, tubes, and lamps including fluorescence have been developed within the photoluminescence. Photoluminescence materials interact with energy transfer, optical emission, photoexcitation, nonradiative, and radiative energy relaxation (Su et al., 2020).

Related to the time, luminescent materials can generate as an output two phenomena which are fluorescence and phosphorescence. If the output can produce in 10^{-8} seconds after the input which is called fluorescent materials, the output can take more time which is known as phosphorescent materials. The process depends on a material deficiency, time, and frequency of the reconfiguration (Nag Bhargavi and Khare, 2015). Fluorescence, which is spontaneous emission takes place with the absorption of a photon, after the emission the first singlet state S1 excitation occurs and the spin multiplicity does not change with fluorescence. After the intersystem crossing from S1, radiation can be emitted with the triplet state T1, which is called phosphorescence and spin multiplicity can change with this phenomenon. This is known as the Simplified Perrin-Jablonski diagram which is shown in Figure 3.

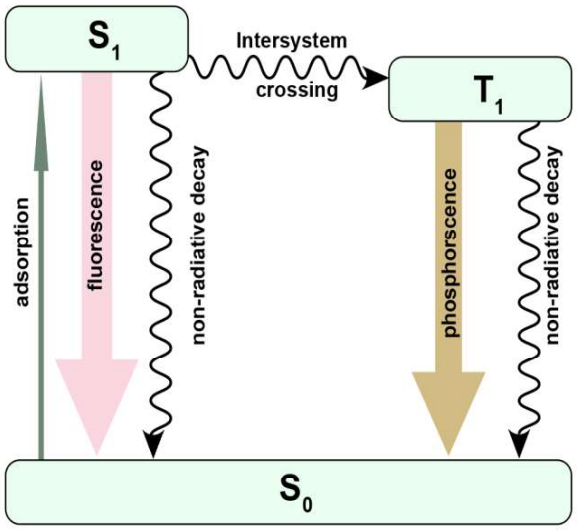

Figure 3. Fluorescence and phosphorescence difference in Simplified Perrin-Jablonski diagram (Source: Valeur and Berberan-Santos, 2012)

With the emission of phosphorescence, electrons transmit to triplet excited states from singlets excited states, and its spin cannot be at the ground state as in the beginning.

The fluorescence spectrum is usually similar to the first absorption band because differences between the vibration levels in the ground and excited states are similar, which is called the mirror image rule (Valeur and Berberan-Santos, 2012). So, the gap between the maximum value of the first absorption band and the maximum fluorescence value is called the Stokes shift and this shift is expressed by the wavenumber given in Figure 4 (a). If an excited photon was emitted in less energy, this is related to the stokes shift but, after the absorption of two or more low energy photons, it can be luminescent excitation with higher energy which is called anti-stokes shift.

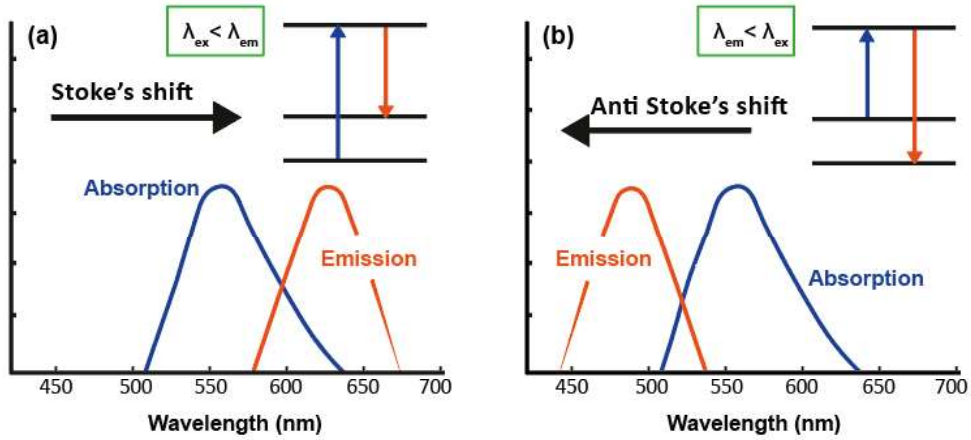

Figure 4. Luminescence phenomenon based on (a) stokes shift and (b) anti-stokes shift (Source: Khodabakhsh, 2018)

For this purpose, upconversion is a nonlinear phenomenon and the working principle is related to anti-stokes emission and the low energy photons having the higher energy are excited (Zhou et al., 2015) which is given in Figure 4 (b).

Upconversion based on lanthanides are classified as regards, excited-state absorption (ESA), energy transfer upconversion (ETU), cooperative upconversion (CUC), photon avalanche (PA), energy migration-mediated upconversion (EMU), and lastly cross-relaxation (CR) (Zheng et al., 2019) and YVO_4:Er, $NaYF_4$:Yb, Er, Y_2O_2S:Er, etc. can be given as some examples for lanthanide-doped upconverting materials (Zhou et al., 2015). The ESA mechanism works in which a single ion (I) in the ground state goes through the excited state with high energy for lanthanide-based materials. Also, ETU having a similar process with ESA is absorbed by photons excitation with the higher levels.

Zwinkels and Canada (2016) reported the electromagnetic spectrum of colors are in order of violet (400-430 nm), blue (430-480nm), green (480-560nm), yellow(560-590nm), orange(590-620nm) and red (620-700 nm). The minimum number of photons is related to upconversion intensity (I_E) and laser power. For example, if there is an emission of 378 nm, and the laser power (P^n) is approximately 976 nm, the minimum photon number (n) can be calculated n=976/378 is equal to 3 with the relation of upconversion intensity (Kumar, 2011) The relation is that;

$$I_E \propto P^n$$

Equation 1. Relation of Upconversion intensity (I_E) with power of the laser pump (P) and the minimum number of photons (n)

Tm^{3+}-Yb^{3+} and Er^{3+}-Yb^{3+} co-doped K-LTO and their upconversion properties were reported by Sağlam (2020). RP type K-LTO optimized and analyzed with Tm^{3+}/Er^{3+} (activators) -Yb^{3+} (sensitizer) with different co-doping concentration.

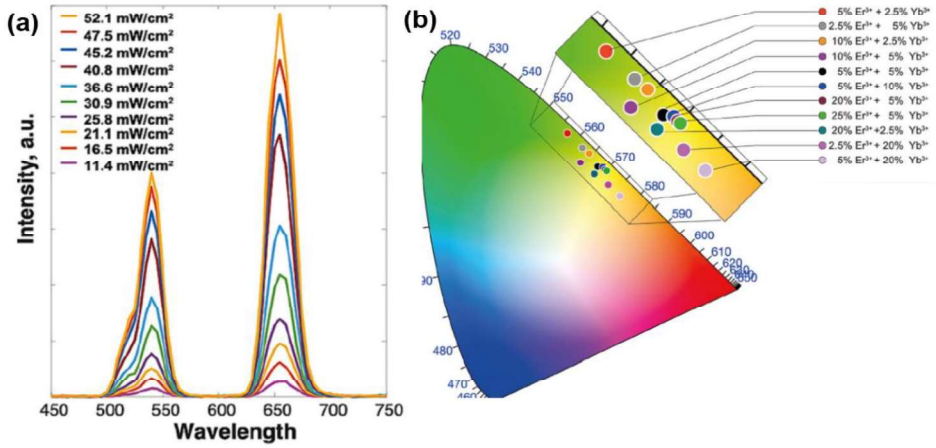

Figure 5. (a) UC emissions of 2.5%Er^{3+}-5%Yb^{3+} co-doped K-LTO with different laser power and (b) CIE diagram for different concentrations of Er^{3+}-Yb^{3+} co-doped K-LTO. (Source: Sağlam, 2020)

In Figure 5 (b) 5%Er^{3+}-2.5%Yb^{3+} co-doped K-LTO showed the intense green color located in the CIE diagram compared to other layered perovskites. From lower dopant to higher dopant concentrations of Er^{3+}-Yb^{3+}, green color ($^2H_{11/2}$, $^4S_{3/2}$ → $^4I_{15/2}$ transitions) shifted to red color ($^4F_{9/2}$ → $^4I_{15/2}$ transition) Besides that, there is a significant increase from 11.4 mW/cm^2 to 52.1 mW/cm^2 laser power application for UC emission changes given in Figure 5(a). For this reason, RP type 5%Er^{3+}-2.5%Yb^{3+} co-doped K-LTO was chosen for the nanofilm fabrication.

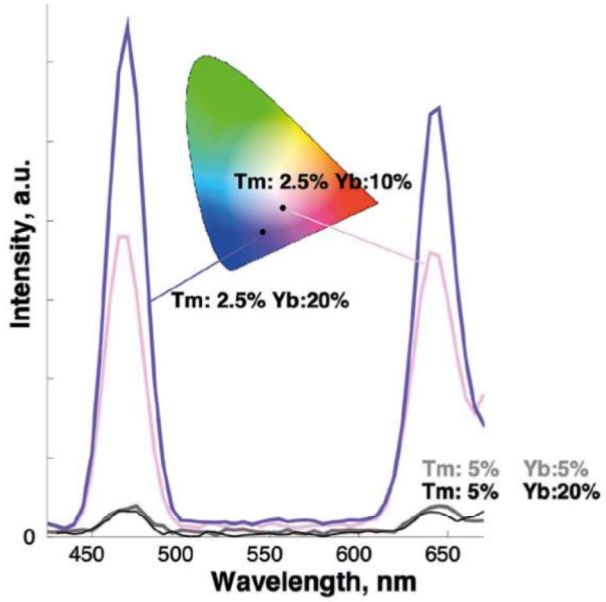

Figure 6. Different concentrations of Tm^{3+}-Yb^{3+} co-doped K-LTO, UC emissions and represented CIE diagram (Source: Sağlam, 2020)

2.5%Tm^{3+}-20%Yb^{3+} co-doped K-LTO showed the blue color located in the CIE diagram. Blue emission was observed at 470 nm ($^1G_4 \rightarrow {}^3H_6$ transition) and the red emission was observed at 645 nm ($^1G_4 \rightarrow {}^3F_4$ transition) which is shown in Figure 6. In this thesis, Er^{3+}-Yb^{3+} and Tm^{3+}-Yb^{3+} co-doped RP-type perovskites were studied because of their upconversion emissions in the blue, green, and visible regions. Different Tm^{3+}-Er^{3+} co-doped K-LTO concentrations were synthesized to detect emission in the red region.

2.4. Biological Applications for Layered Perovskites and 2D Nanomaterials

Nanotechnology is a multidisciplinary field having an extensive biological application area for specifically therapeutic studies, vector transfections, antimicrobial agents, fluorescent labels, and cytotoxic perspectives(Uygur et al., 2009). Design and manipulation of materials in nanoscale develop the novel engineered nanomaterials and their bulk, other-dimensional forms can be elucidated for their unique properties in chemical, biological, mechanical, and physical aspects (Liao et al., 2018). Nanomaterials can be applicable for biological studies because of their smaller size and properties after the understanding of their biocompatibility. Related to *in-vitro*

studies, nanomaterials especially can be taken up by cells easily. For this purpose, the nanomaterials have to be detailed clearly because of cell-nanomaterial interaction for biological applications such as cytotoxic, antimicrobial, etc.

Toxicity for nanomaterials can be tested with *in-vitro* and then *in-vivo* assays. Cytotoxicity can be analyzed with tetrazolium salt-based MTT (3-(4,5-dimethylthiazol-2-yl)- 2,5-diphenyl-tetrazolium bromide), XTT (2,3-bis- (2-methoxy-4-nitro-5-sulfophenyl)-2H-tetrazolium-5-carboxanilide)), MTS (3-(4,5-dimethylthiazol-2-yl)-5-(3-carboxylmethoxyphenyl)-2-(4-sulfonyl)-2H-tetrazolium)), WST-8 (water-soluble tetrazolium salt 8) and WST-1(water-soluble tetrazolium salt 1) assays. MTT is the most widespread assay for analysing cell viability, cytotoxicity and proliferation studies (Nogueira et al., 2014).

2D carbon nanomaterials are of great interest in biosensors, drug delivery, and bacterial inhibition which are related to biomedical studies. The graphene oxide (GO) nanosheets showed the lowest hemolytic activity compared with larger GO and sonicated GO. The cytotoxic response was quite high for cationic nanoparticles which are 60 nm NH_2-labeled polystyrene (PS) nanospheres using five different cell lines reported by Xia et al.,(2008).

Zhang et al.,(2012) reported that rare earth metals (REM) can be used for anti-tumor and immune regulation. Also, rare earth compounds have been reported as selectively inhibiting or killing the tumor cells in the minimum effect of toxicity (Shi and Huang, 2005; Xu et al., 2011). Lanthanides can reduce apoptosis in several cells (Wu et al., 2013). Liu et al., (2010) studied the effect of lanthanum chloride on cell proliferation and migration using human cervical cancer (HeLa). Yu et al., (2015) reported that lanthanum chloride ($LaCl_3$) treatment has been shown to inhibit HeLa cell proliferation and decrease tumor weight. Also, lanthanum citrate ($C_6H_5LaO_7$) complex has been demonstrated novel therapy of cancer cells which is proved using HeLa cells and showed the low concentration of lanthanum citrate complex has caused of apoptosis by the Caspase-9 activation and increased of pro-apoptotic protein Bax expression (X. Su et al., 2009). Related to lanthanum ion (La^{3+}) and compound studies, that have exhibited biological effects for cancer cells with different pathways as a single target or multi targets such as a target for siRNA which reported by Li et al., (2020)

Ansari et al., (2020) compared the potential of MCF-7 and A-549 cell lines cytotoxicity using lanthanum oxide (La_2O_3) activated with Pr- and Eu- differently. It showed that La_2O_3: Eu and La_2O_3: Pr could be more toxic for the A549 cell lines. However, the results are related to an increase in REM (Rare earth metals) concentrations. 100 µg/ml lanthanum complex addition showed 80-50% cell viability for all MCF-7 and A549 cell lines. Particle shape, size, surface properties, small grain size, and the excellent surface-to-volume ratio of nanomaterials can be affected for the toxicity and biocompatibility (Ansari et al., 2020)

Structure of $SrTiO_3:Tm^{3+}/Yb^{3+}$ nanopowders was used for the in vitro nanoparticle cytotoxicity using J774.E murine macrophages and U2OS human osteosarcoma cell lines. It was also shown that this kind of nanoparticles does not damage the red blood cells in 100 µg/ml concentration. However, U2OS osteosarcoma cells decreased after 10 µg/ml concentration of $SrTiO3:Tm^{3+}/Yb^{3+}$ which is selective toxicity. In this respect, not only nanoparticle size, properties but also cell sensitivity and release of ions in the medium can be affected by the toxicity. Different cells could be shown the different effect of viability (Pazik et al., 2016)

Kale et al., (2006) studied with different concentrations of lanthanum from $La_{0.7}Sr_{0.3}MnO_3$ (LSMO) nanoparticles and doped with cerium (Ce) and they showed when lanthanum concentration increases stoichiometrically, cell viability could be decreased. They were used in human fibrosarcoma (HT-1080) and human skin carcinoma (A-431) cell lines. Generally, lanthanum mole numbers between 0.3-0.5 could not be affected for the cells and it was shown 50-80% cell viability but cell toxicity could be increased when using a high concentration of lanthanum in stoichiometric ratio. Ce doped LSMO could be showed low cytotoxicity. In the body, liver, and kidney are the organs that have an accumulation of toxic metabolites (Yang et al., 2016) Bulk form of layered perovskites and nanoparticle form of exfoliated layered perovskites can have different properties such as optical and electrical properties (Ma and Sasaki, 2010).

In this thesis, the cell viability was analyzed using MTT assay for layered RP type perovskites and their 2D nanosheet forms. The effect of 2D nanosheets on cell viability was examined using cancer cell lines and normal cell lines. Live and dead cells were visualized with fluorescent microscopy using the Cell Health Assay Kit.

CHAPTER 3: METHODOLOGY OF EXPERIMENTAL DESIGN

3.1. Synthesis of Layered Perovskites

The Ruddlesden-Popper type of $K_2Ln_2Ti_3O_{10}$ was the main chemical compound for the synthesis of 3D layered perovskites (Ln: La^{3+}, Tm^{3+}, Er^{3+}, Yb^{3+}). The layered perovskite $K_2La_2Ti_3O_{10}$ (K-LTO) was synthesized by conventional solid-state procedure (Sağlam, 2020)(Taniguchi et al., 2014). Lanthanum (La^{3+}) was doped with other lanthanide combinations, separately (Yb^{3+}-Er^{3+}, Yb^{3+}-Tm^{3+}, and Tm^{3+}-Er^{3+}). K-LTO were mixed in different stoichiometric amounts because of doping with Tm^{3+}-Er^{3+} shown in (Table 2. Tm^{3+}/Er^{3+} co-doped K-LTO). Er^{3+}-Yb^{3+} doping with 2.5%Er^{3+}-5%Yb^{3+} concentration and Tm^{3+}-Yb^{3+} doping with 2.5%Tm^{3+}-20%Yb^{3+} concentration was studied.

20 mol % excess potassium carbonate (K_2CO_3, Sigma-Aldrich 99.99%), lanthanum (III) oxide (La_2O_3, Sigma-Aldrich 99.99%), titanium dioxide (TiO_2, Sigma-Aldrich 99.99%), erbium (III) oxide (Er_2O_3, Sigma-Aldrich 99.99%), thulium (III) oxide (Tm_2O_3, Sigma-Aldrich 99.99%) and Ytterbium (III) oxide (Yb_2O_3, Sigma-Aldrich 99.99%) chemicals were used for the preparation of layered perovskites. The amounts of chemicals were weighed on the analytical balance. The annealing was carried out for the synthesis of material reported by Taniguchi et. al. (2014). The chemical mixture was mixed in the mortar for 30 minutes and after that added into the platinum (Pt) crucible. The crucible was put in the ash furnace for calcination. The solid-state reaction was applied in two steps. Firstly, the chemical mixture was annealed at 900 ºC 4 h. After cooling down the products were mixed in the mortar for 30 minutes again and annealed at 1100ºC 11 h. Some synthesis materials were annealed 1000ºC 4 h - 1200ºC 11 h in the air in the ash furnace to understand the temperature effect (other parameters and studying conditions unchanged). The powders were put in the glass tubes and the Pt crucible was cleaned with 15 minutes 5M HCl and 15 minutes ultra-pure water in the sonicator.

3.2. Ion Exchange of Layered Perovskites

Ion exchange was performed using 1.0 g the synthesized layered perovskite powders interacted with 100 ml of aqueous HCl solution. For this purpose, acid

concentration was optimized in the first step. The layered perovskite powders were treated with 0.5M, 1M, and 3M HCl in an aqueous solution. This process was continued with shaking for 7 days at room temperature and each day acid exchange was repeated adding the same amount of HCl solution by using centrifugation (15 min - 4000 rpm). End of the protonation, solid products were collected and cleaned from HCl solution with washing ultra-pure water. At the end of protonation, samples were analyzed with characterization methods. The molarity of acid concentration was comprehended with XRD patterns and their SEM images for these layered perovskites. 0.5M HCl concentration was used in all subsequent studies.

3.3. Synthesis of 2D Nanosheets

Exfoliation was started for the conversion of nanosheets by using protonated pellets. A weighted amount (0.4 g) of the protonated form was reacted with some chemical solutions which are shown in table 2.

Table 2. Exfoliation parameters

Protonated sample / TBA solution volume	Solutions for Exfoliation	Shaking Time and Speed
0.4 gr / 100 ml	$TBAOH^-/H^+$ = 112/1 (n/n)	7 Days - 120 rpm
0.4 gr / 100 ml	$TBAOH^-/H^+$ = 74/1 (n/n)	7 Days - 120 rpm
0.4 gr / 50 ml	EA^-/H^+ = 4/1 (n/n) $TMAOH^-/H^+$ = 2/1 (n/n) $TBAOH^-/H^+$ = 2/1 (n/n)	7 Days - 80 rpm 7 Days - 80 rpm 7 Days - 80 rpm
0.1 gr / 20 ml	$TBAOH^-/H^+$ = 8/1 (n/n)	7 Days - 120 rpm

Firstly, exfoliation was carried out by shaking at 120 rpm for 7 days with 1.5M and 1M 40%(Sigma Aldrich) tetrabutylammonium solution ($TBAOH^-$) separately for 7 days at room temperature. After the end of the time, the exfoliated solutions waited vertically for sedimentation of the solid part. The supernatants were collected from the solution as the nanosheet solutions. In this case, when 1.5M TBAOH- solution was used, the mole ratio of the protonated sample was determined as H+/TBAOH-(n/n):112. It has been understood that this ratio has been successful for the production of nanosheets. A total of 21 days of treatment was carried out with ethylamine (EA)

solution, tetramethylammonium hydroxide (TMAOH) solution, and TBAOH solution shown in Table 2, however this method was not showed the nanosheets. The exfoliation process was shown in Figure 7.

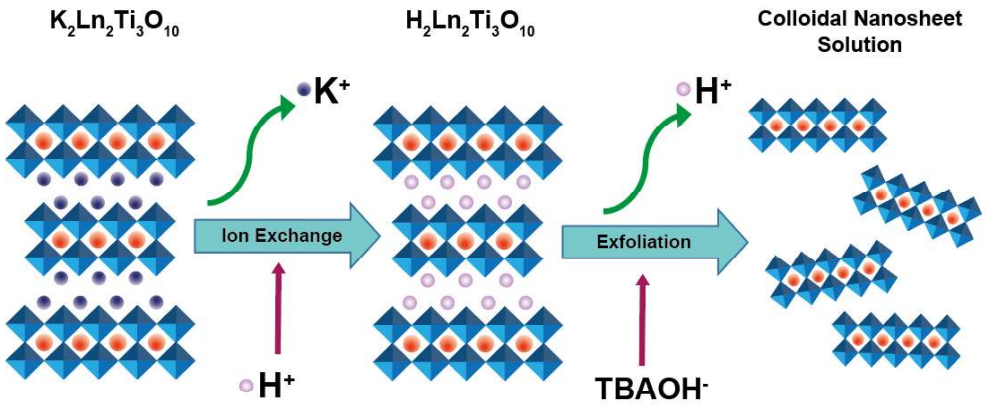

Figure 7. Colloidal nanosheet solution process from layered RP perovskites

3.4. Fabrication of Nanofilms

Nanofilms were fabricated by layer-by-layer (LBL) method using an automated dipping system. All substrates (Quartz, ITO/Glass) were cleaved to the approximate dimensions of 1 by 2 cm. Quartz substrates were cleaned using acetone, isopropanol, and ultrapure water for 15 min in the ultrasonic cleaner, respectively. The substrates were dried with 99.9% ultrapure nitrogen gas. The nanofilm fabrication was prepared using automated dipping system which is shown in Figure 8.

Figure 8. Automated Dipping System

The first coating method took place between immersion of 2 wt% poly diallyl dimethylammonium chloride (PDDA) 3 minutes and immersion of nanosheet solution 15 minutes. All these steps were repeated in 20 deposition cycles that were covered on the quartz surface. Negatively charged nanosheets were attracted with positively charged PDDA on the quartz substrates.

Table 3.The 20 times of nanosheet coating for the nanofilms in quartz substrate

Nanosheet Solution	PDDA Solution Holding Time	Nanosheet Solution Holding Time	PDDA solution in water
$La_{1.85}Er_{0.05}Yb_{0.1}Ti_3O_{10}$	3 min	15 min	2 gr/ 100 mL
$La_{1.55}Tm_{0.05}Er_{0.4}Ti_3O_{10}$	3 min	15 min	2 gr/ 100 mL
$La_{1.55}Tm_{0.05}Yb_{0.4}Ti_3O_{10}$	3 min	15 min	2 gr/ 100 mL

When their upconversion emissions were analyzed, their intensities were weak so the nanofilm coating method changed for the ITO-coated glass substrates. Nanofilm coating studies were performed on ITO/glass (Rs<15W/A) substrate. ITO/glass substrates were cut dimensionally 1cm x 2cm and cleaned with acetone, ethanol, and ultrapure water for 10 minutes. In order to detect the coating of nanosheets on ITO/glass substrate, the coatings were analyzed in UV/VIS/NIR spectrophotometer between 250-800 nm wavelength after each coating. Coatings were prepared with the following steps by slightly changing the above method by soaking in a PDDA solution

for 3 minutes and soaking in a nanosheet solution for 15 minutes illustrated in Figure 9.

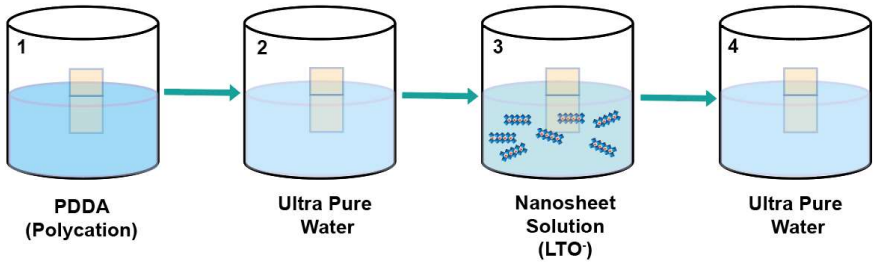

Figure 9. LBL nanofilm coating process

The second coating method in which ITO/glass substrates waited in 2.5g/100ml PEI (Polyethyleneimine) solution for 20 minutes before nanofilm coating. The purpose of this is to make the surface positively charged to prepare the material for nanofilm coating. After the positively charged substrate was dried with 99.9% ultrapure nitrogen gas, then the substrate was immersed in the nanosheet solution and left for 20 minutes in the colloidal nanosheet solution(Sasaki et al., 2001).

This method was performed with respect to a nanosheet solution, ultrapure water, PDDA solution, and ultrapure water using an automated dipping system similar to the previous coating method, respectively. Moreover, absorbance changing due to the increase of coating using the spectrophotometer was investigated.

Tm^{3+}-Er^{3+}, Er^{3+}-Yb^{3+}, and Tm^{3+}-Yb^{3+} co-doped LTO nanosheets were coated as 20 sequences, 30 sequences, and 60 sequences. For the device fabrication, a portion of ITO was etched using the procedure described below to avoid leakage current prior to nanofilm production. The design of the multifunctional device was given in Figure 10.

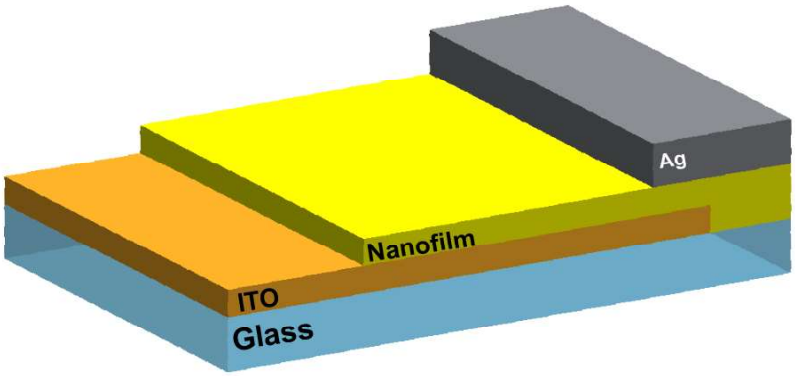

Figure 10. Design of the device with nanofilm on ITO/glass substrate

Etching the ITO from the glass substrate surface was performed except for the area to be removed, other parts were covered with tape. Some Zn powder was added to the ITO, which was not covered with tape, and it was dissolved with 5 M HCl. After waiting for about 30 seconds, the etched part was cleaned with a dust-free napkin. Thus, ITO was removed from the surface. The process of substrate preparation for device design was shown in Figure 11.

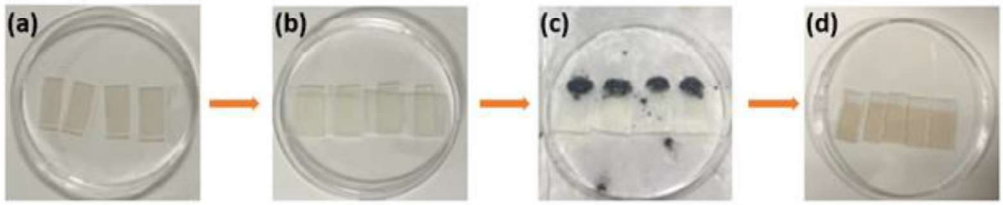

Figure 11. The process for removing ITO (a) ITO coated glass substrates (b) Covering a part of the surface with the help of tape (c) Etching ITO from the surface with Zn powder and acid (d) The result of removing ITO from the glass surface

3.5. Characterization of Layered Perovskites, 2D Nanosheets and Nanofilms

Characterization is the most important step for nanotechnological studies. They have the smallest sizes and atomic detection of physical and chemical differences. In this aim, the synthesized and protonated powders were analyzed with XRD for understanding crystallization of layered materials, their powders were captured with

SEM analysis for their 3D shape morphology, AFM was used for morphology and height determination of 2D nanosheets and nanofilm and powder form of synthesized layered perovskites, 2D nanosheet forms, and their nanofilm coatings were analyzed in UC hand-made measurement.

3.5.1. Atomic Force Microscope Analyzes

SPM (Scanning Probe Microscope) is one of the most effective methods of modern research techniques, which allows the examination of the regional characteristics and morphology of samples with high resolution. Rohrer, Binnig and coworkers invented a brand technique of the probe microscope which is name STM (Scanning Tunneling Microscope), and the following years (1986s) Binnig, Quate, and Geber had established AFM (Atomic Force Microscope), is a historic moment for nanoscience and nanotechnology (Tomczak et al., 2011). AFM as also known as scanning force microscopy (SFM) has the ability of real atomic and molecular resolution which can also be biological samples even in liquid (Yamasue et al., 2009). The working principle of AFM includes forces (interatomic forces, electromagnetic forces) between two parts (tip and sample) very close to each other and generally, this distance can be from a few nanometers to tens of nanometers on a very small scale (Bramowicz et al., 2012). It can be used for characteristic samples which are conductors and insulators.

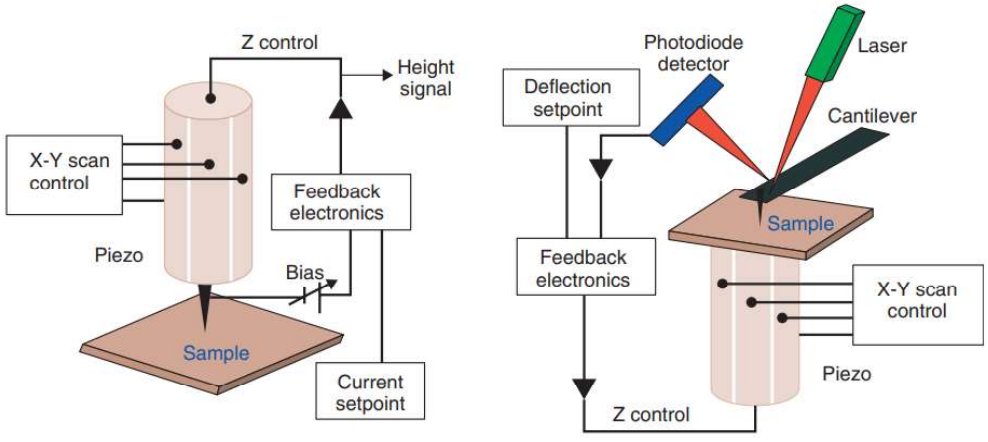

Figure 12. 3D configuration of STM (1st) and AFM(2nd) Setups (Source: Allison et al., 2010)

The AFM mechanism is based on the detection of forces between the AFM tip and the specimen on the surface which is shown in Figure 12. Generally, it can be separated into three parts: computer, control electronics, and microscope. Likewise, it includes tip, sample, cantilever, controller, photodiode detector, piezo tube scanner, laser. AFM probes and cantilevers are commonly fabricated with silicon-based microfabrication techniques; for example, Si, SiO_2, Si_3N_4 can be produced (Tsukruk, Davies and Philip, 2012). AFM tips can be classified into three basic geometries: pyramidal, conical, and tetrahedral (Tsukruk, Davies and Philip, 2012). The coating on the tips can be changed depending on the mode of the desired measurement. For the electrical measurements, the thin films of PtIr, TiN, Au, and Pt are coated on the tips; CoCr, FeNi, Co, and SmCo thin film coating is used for magnetic measurements.

Tip-surface distance can affect its attractive and repulsive forces and magnitude of the force when the tip is approaching the sample surface (Bramowicz, Kulesza and Rychlik, 2012).

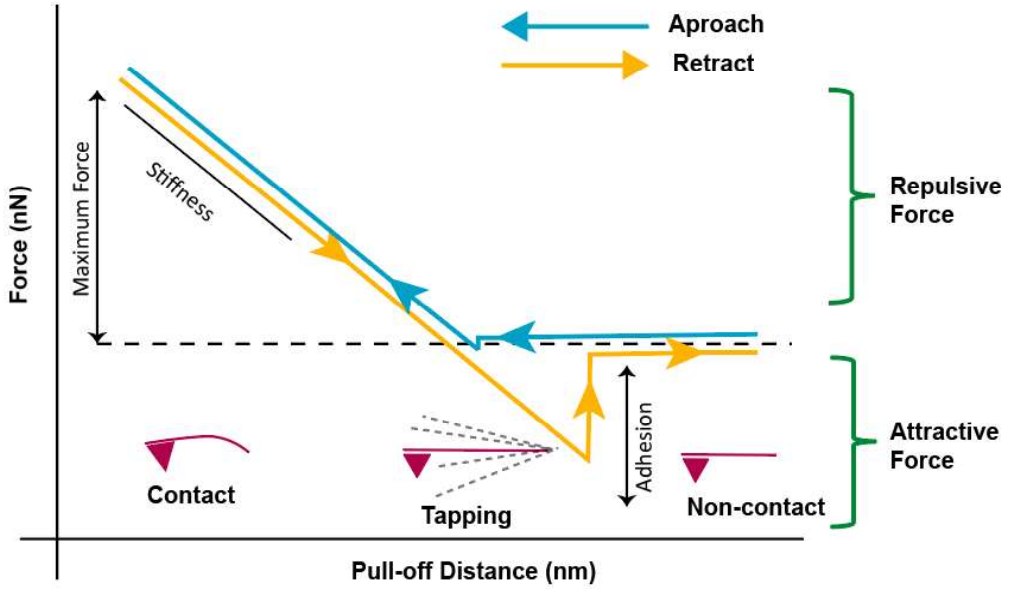

Figure 13. Forces between AFM tip and scanned sample surface (Source: Bramowicz, Kulesza and Rychlik, 2012; Maver et al., 2013)

As shown in Figure 13, interaction forces are related to the long-range attractive regime which is the non-contact mode, and the short-range repulsive regime which is the contact mode. Attractive forces include not only Van der Waals interactions, but also electrostatic forces additionally, hydrogen bonding, charge transfer interactions, etc. Repulsive forces also included electrostatic forces as well as Coulombic interactions (Tsukruk, Davies and Philip, 2012).

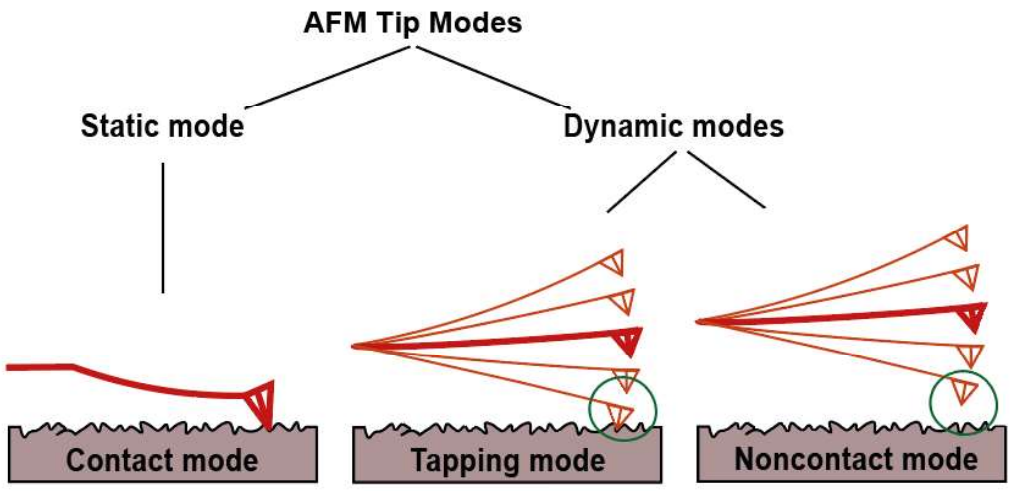

Figure 14. AFM operation modes

Based on scanning dynamics, AFM operation can be divided into a static and dynamic mode shown in Figure 14. Briefly, dynamic modes involve oscillating and motions on the cantilever (vertical or lateral), usually related to its resonance frequency. The tip and the sample affect due to the resonant frequency, amplitude, and phase of the oscillation, under dynamic conditions. Dynamic modes can be divided into several modulations, the most common modulations of amplitude modulation (AM-AFM) and frequency modulation (FM-AFM). Dynamic forces can be classified as a tapping mode and non-contact mode. Tapping mode is the most common type of dynamic AM-AFM (Tsukruk, Davies and Philip, 2012).

The thickness and lateral size of nanosheets were determined by the Hitachi 5100N Atomic Force Microscope (AFM). Hitachi multifunction SPM unit AFM 5100N (Figure 15) was used with its software probe station AFM 5000II as an AFM measurement. The features of Multi75Al-G tip, it has rotating shape, 15-19 um height and 10-20 um set back in the less than 10 nm radius which is regarded as 20-25 o along

cantilever. The cantilever features have a beam shape, 215-235 um length, 2-4 um thickness. The cantilever works parameters are 3N/m force constant and 75 kHz frequency.

Figure 15. Hitachi multifunction SPM unit AFM 5100N

The Q curve defines the resonance characteristic of cantilever which can be controlled before starting to scan and shows that the tip and cantilever received the laser properly. ADD value is observed at 7.5 to 7.9V for the Multi 75Al-G tip. The AFM tuning mode is set in automatic or manual mode depending on scanning. ITO/glass, quartz, and mica substrates were used to determine 2D nanosheets or layer-by-layer coated nanofilms.

3.5.2. X-Ray Diffractometer Analyzes

X-Rays are used for biomedical imaging, radiotherapy, and medicine as targeting or treatments, etc. X-ray diffraction (XRD) was discovered by Max von Laue during the development of X-Rays in 1912. The mathematical mechanism of XRD is known with Bragg law related to crystal forms. There are some X-ray diffraction techniques such as; Single-crystal X-ray diffraction (SCD), X-ray powder diffraction (XRPD), small-angle X-ray scattering (SAXS) and wide-angle X-ray scattering (WAXS), etc. The lattice points of crystals having importance can arrange the three-dimensional structure for atoms and lattices can be formed of unit cells. Also, unit cells

for three vectors and angles can be determined as “a,b and c” and “alpha, ß and ɣ “, respectively. If the a = b = c and alpha= ß = ɣ = 90 degree it is regarding ideal cubic system and equal lengths and perpendicular for each other. The crystal forms of lattices and their configurations can be cubic, tetragonal, hexagonal, trigonal, orthorhombic, monoclinic and triclinic structures Interplanar spacing (d_{hkl}) and miller indices (*hkl*) are having a relationship which is also important parameters for Bragg law (Dierickx et al., 2011).

This mechanism is related to monochromatic X-ray beams because the X-ray beam reaches a sample and there can be some absorption or some electron attraction but generally the beam can be scattered in the same wavelength. Even if some equations and relations represent between sample structure and diffraction patterns, Bragg law defines that in the simplest way which is shown in Equation 2.

$$n\lambda = 2\sin\Theta$$

Equation 2. Bragg’s Law for the crystal planes

The X-rays come in the crystal planes with incident angle Θ and scatters with reflection angle Θ. lambda represents the wavelength, n is the integer number, and d expresses distance of adjacent planes. d can be calculated using equation 2 with miller indices information. In this case, the diffraction peaks are becoming known given in Figure 16.

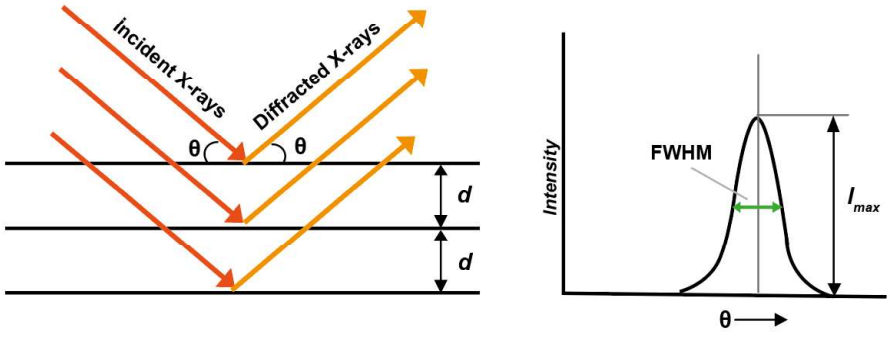

Figure 16. X-Ray diffraction (a) at the Bragg angles, (b) diffraction peak and its intensity (Source: Dierickx et al., 2011)

The X-ray peaks can be affected by the material strain, structure or size, thermal vibration, ambient-instrumental conditions, X-ray beam features (size, variance, spectra motions and resolution of detector etc.). The full width at half

maximum (FWHM) determines the peak width and I_{max} represent the maximum intensity of the peak.

The crystal structure of the layered perovskites was analyzed by X-ray diffraction patterns. Panalytical Empyrean X-ray diffraction (λ = 1.5406 Å) with Cu Kα radiation was used.

3.5.3. Scanning Electron Microscope Analyzes

Scanning electron microscope (SEM) is one of the types of microscope techniques for analyzing specimen surfaces. In the vacuum chamber, electron beams go through specimens with the help of electromagnetic lenses. These lenses focus the electrons directly to specimens and selection detectors collect the scattered electrons which are emitted signals from the specimen. Generally, 15-30 keV electrons can be used and the SEM chamber can be settled to 0.1-10 $^{-}$4 Pa vacuum pressure. The schematic of SEM is shown in Figure 17.

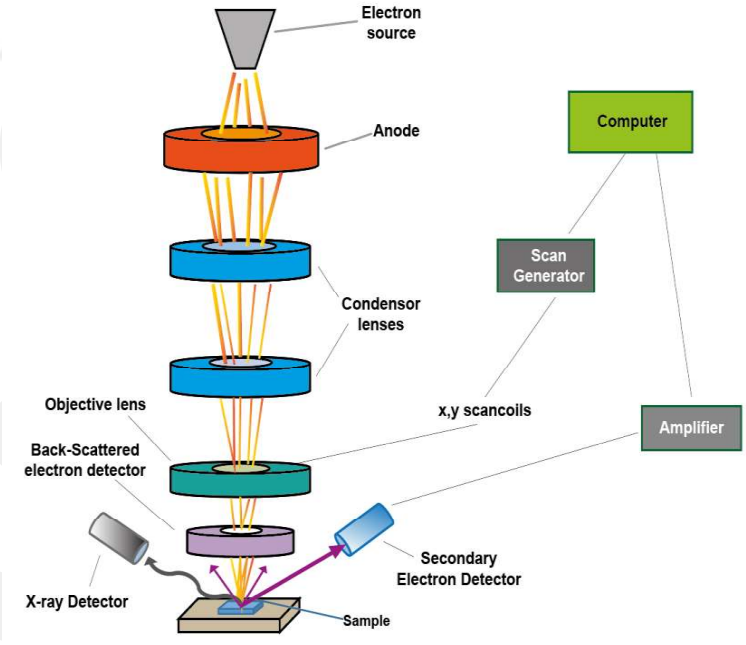

Figure 17. Schematic of SEM mechanism (Source: Inkson, 2016)

Carl Zeiss 300VP and Hitachi TM4000 SEM instruments were used for the 3D morphology of powder layered nanomaterials and their protonated forms.

3.5.4. Upconversion Measurements

A monochromator is an optical device used to detect narrow bands of light over a wide range of wavelengths. Monochromators have been incorporated into many optical measuring instruments and systems. A monochromator can be combined with an optical detector. That can be used to detect the spectral power distribution (SPD) of light sources, reflection or transmission of samples, etc. Monochromators are important for color measurements, as color-related optical properties are wavelength-dependent. If the light comes out of the monochromator and illuminates the sample, the incident light is called monochromator light. If a monochromator is used after the light reflected on the sample, monochromatic signals are formed at that point. The operation of a typical spectrometer is also based on this logic (Chuang, 2016). The schematic of the monochromator and UC instrument is given in Figure 18.

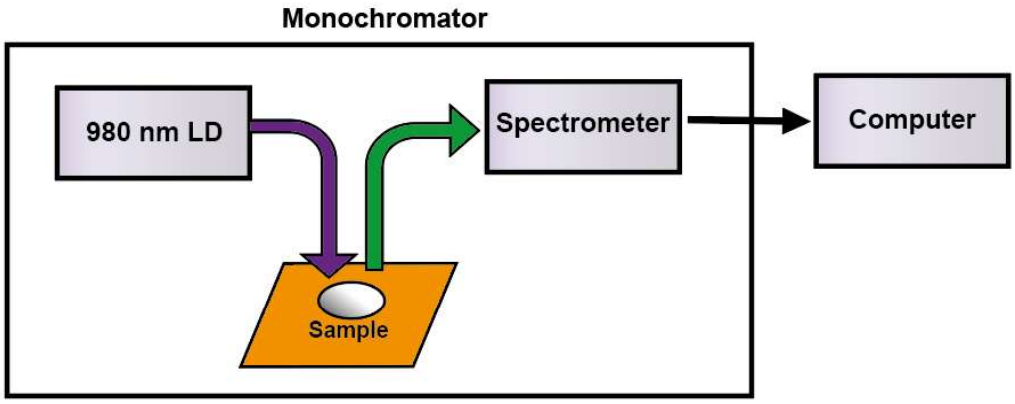

Figure 18. Schematic of UC instrument (Source: Chuang, 2016)

The intensity of powder co-doped layered perovskites, 2D nanosheet forms, and their nanofilm coatings were analyzed using handmade setup UC measurement. The excitation source comes from a 980 nm NIR laser diode (LD) and is collected from Thorlabs PDF 10A/M detector. Cornerstone 130 ⅛ monochromator was used for the analyzing of excitations and all samples were measured at room temperature.

3.5.5. Spectrophotometer Analyzes

Perkin Elmer UV/VIS/NIR spectrophotometer was used for analyzing the number of coatings onto the ITO/glass substrate. For this reason, a scanning method was performed which is from 250 nm to 800 nm in the instrument software. Solid ITO/Glass substrates were coated layer-by-layer method and each coating was analyzed with a spectrophotometer using a solid sample holder.

3.6. Animal Cell Culture Studies and MTT Assay

HEK 293 (human embryonic kidney) and HepG2 (human hepatocellular carcinoma) were provided by Prof. Dr. Esra ERDAL from Izmir Biomedicine and Genome Center. HEK 293 and HepG2 cells were cultured in a 5% CO_2-fed incubator at 37ºC in the DMEM (Dulbecco's Modified Eagle's Medium) and RPMI 1640 mediums, respectively with the addition of 10% fetal bovine serum in each medium.

K-LTO, Tm^{3+}-Er^{3+} co-doped K-LTO powder samples were prepared with 10 mg powder mixed with 10 ml ultrapure water as a 1 mg/ml stock solution. Nanosheet forms of non-doped LTO and Tm^{3+}-Er^{3+} co-doped LTO in the TBAOH solution were precipitated to be 10 ml nanosheet solution/20 ml 5M HCl solution (v/v). After the addition of acid into the nanosheet solution, the mixing was sonicated for 15 minutes. For the collecting of precipitated nanosheets, centrifugation was used at 14000 rpm for 15 minutes, then the pellet form of nanosheets was separated from the solution and washed six times with ultrapure water for removing acid mixing.

MTT(3-[4,5-dimethylthiazol-2-yl]-2,5-diphenyltetrazolium bromide) assay, which is one of the colorimetric methods, was used to determine cell viability. The MTT assay enables the determination of mitochondrial activity in living cells and the cytotoxic properties of the treated molecules by comparing them with the control group (Mosmann, 1983). Cell viability was assessed with MTT assay as follows: HEK 293 and HepG2 cells were seeded 96 well flat-bottom plates with initial cell concentration of $3x10^4$ in 200 µL/per well and overnight incubated in medium with 10% FBS at 37ºC in an atmosphere of 95% humidity with 5% CO_2 . After 24 hours, the mediums in the wells were changed with the serial dilutions of nanoparticle concentrations from 100 µg/ml to 10 µg/ml which mixed in fresh mediums. Cells were exposed to the nanoparticles for 48 hours in the incubator. Changes in cell morphologies were observed with light microscopy (Euromex Oxion Inverso) and the cell pictures were taken with its digital camera equipment. End of the 48 hours, the MTT labeling reagent was added to wells 30 µL/per well from 5mg/ml stock solution and incubated for 4 hours in the same conditions. Then, mediums were aspirated from the wells carefully because of preventing formazan crystals damages to the cells (Twentyman PR and Luscombe M, 1987). Each well was treated with 80 µL DMSO for 30 minutes because of dissolving formazan crystals. End of the 30 minutes, the cell viability was measured by a microplate reader (Thermo Scientific Multiskan Go, USA) at 570 nm.

Cell Health Assay Kit (Cell Signaling Technology Inc) was used for the cell viability measuring with the addition of MTT. The kit includes Calcein-AM and Propidium iodide for live cell and dead cell staining, respectively. HepG2 and HEK 293 cells were incubated with the addition of 20 μg/ml powder and nanosheet forms of nanomaterials with a control group of cells for 1 hour at 37 ºC. Fluorescent microscope (Olympus 1X71) was performed for cell pictures. For live cells and dead cells were captured at 490-520 nm and 535-620 nm excitation-emission respectively.

CHAPTER 4: RESULTS AND DISCUSSION

4.1. Structural Analysis of Er^{3+}-Tm^{3+} Co-doped Layered Perovskites

The RP type of K-LTO layered perovskites have an I4/mmm space group (No.139) and their lattice parameters in the tetragonal form are a = b = 3.8767 Å and c = 29.824 Å. Also, their angles are α = β = γ = 90◦ because of the having a crystal structure (Silyukov et al., 2018)(Toda et al., 1996). The center of the water ions in the $K_2La_2Ti_3O_{10}$. $2H_2O$ affect its space groups (P4/mmm No.123) and lattice parameters (a=b=3.8585A c=16.814A).

Table 4.Tm^{3+}/Er^{3+} co-doped K-LTO

Sample	Lanthanides Concentration		1.Annealing Condition		2.Annealing Condition	
	Tm %(mol)	Er%(mol)				
$K_2La_{1.9}Tm_{0.05}Er_{0.05}Ti_3O_{10}$	**2.5**	**2.5**	900 °C	4 hours	1100 °C	11 hours
$K_2La_{1.85}Tm_{0.1}Er_{0.05}Ti_3O_{10}$	**2.5**	**5**	900 °C	4 hours	1100 °C	11 hours
$K_2La_{1.75}Tm_{0.2}Er_{0.05}Ti_3O_{10}$	**5**	**5**	900 °C	4 hours	1100 °C	11 hours
$K_2La_{1.7}Tm_{0.2}Er_{0.1}Ti_3O_{10}$	**5**	**2.5**	900 °C	4 hours	1100 °C	11 hours
$K_2La_{1.55}Tm_{0.4}Er_{0.05}Ti_3O_{10}$	**5**	**2.5**	1000 °C	4 hours	1200 °C	11 hours
$K_2La_{1.5}Tm_{0.4}Er_{0.1}Ti_3O_{10}$	**20**	**2.5**	1000 °C	4 hours	1200 °C	11 hours
$K_2La_{1.75}Tm_{0.2}Er_{0.05}Ti_3O_{10}$	10	2.5	900 °C	4 hours	1100 °C	11 hours
$K_2La_{1.55}Tm_{0.4}Er_{0.05}Ti_3O_{10}$	20	2.5	900 °C	4 hours	1100 °C	11 hours
$K_2La_{1.7}Tm_{0.2}Er_{0.1}Ti_3O_{10}$	10	5	900 °C	4 hours	1100 °C	11 hours
$K_2La_{1.5}Tm_{0.4}Er_{0.1}Ti_3O_{10}$	20	5	900 °C	4 hours	1100 °C	11 hours
$K_2La_{1.4}Tm_{0.5}Er_{0.1}Ti_3O_{10}$	25	5	900 °C	4 hours	1100 °C	11 hours
$K_2La_{1.75}Tm_{0.05}Er_{0.2}Ti_3O_{10}$	2.5	10	900 °C	4 hours	1100 °C	11 hours
$K_2La_{1.7}Tm_{0.1}Er_{0.2}Ti_3O_{10}$	5	10	900 °C	4 hours	1100 °C	11 hours
$K_2La_{1.55}Tm_{0.05}Er_{0.4}Ti_3O_{10}$	2.5	20	900 °C	4 hours	1100 °C	11 hours
$K_2La_{1.5}Tm_{0.1}Er_{0.4}Ti_3O_{10}$	5	20	900 °C	4 hours	1100 °C	11 hours

For the structural, spectral analysis and their patterns were investigated using X-ray diffractometer. Tm^{3+}-Er^{3+} co-doped K-LTO was synthesized with different mol

concentration and annealing temperature which is shown in Table 6 and their XRD patterns are shown in Figure 19. Table 6 shows all studies about K-LTO syntheses (co-doped with Tm^{3+}-Er^{3+}) during this thesis. Although blue-colored synthesis showed successful layered morphology, the upconversion (UC) emissions were not demonstrated for having weak intensity.

When the XRD patterns are examined, anhydrous K-LTO in the dominant hydrous phase was observed for 2.5% Er^{3+} - 5% Tm^{3+} co-doped K-LTO and 5% Er^{3+} - 5% Tm^{3+} co-doped K-LTO.

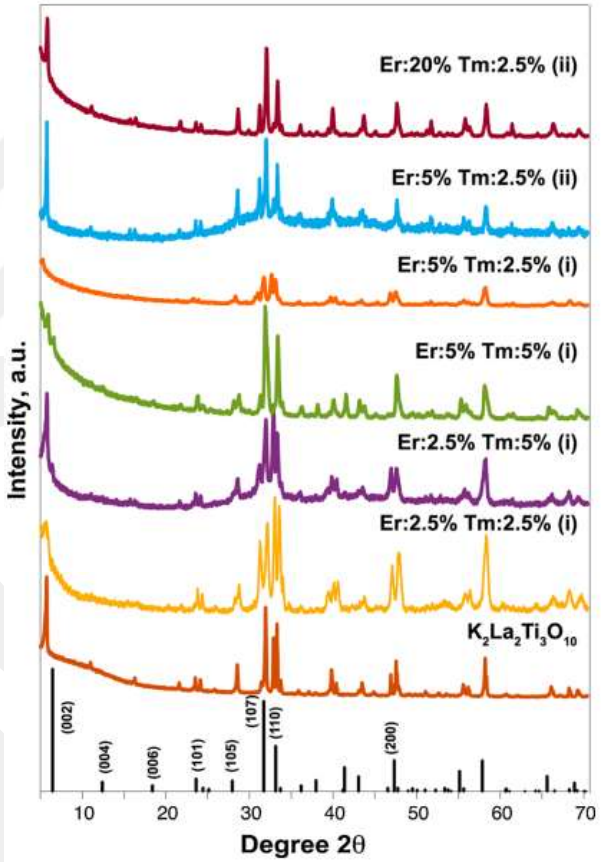

Figure 19. K-LTO co-doped with Er^{3+}-Tm^{3+} XRD patterns (i) 900-1100 ºC synthesis condition (ii) 1000-1200 ºC synthesis condition

Also, the results showed that when the Er^{3+} ions (activator) concentrated from 2.5% to 5% by keeping Tm^{3+}(sensitizer) constant as a 2.5%, (001) peak shifted at a lower angle this is because water ions may be intercalated into the interlayers more than dopant molecules. Thus, less doping concentration can cause more water molecules to enter between interlayer domains. For the comparison of annealing

temperature difference, 2.5%Tm^{3+}-5%Er^{3+} synthesized with 1000-1200 ºC according to step two (ii). Besides that, the results of XRD showed that (001) peak intensity can be higher with high annealing temperature that improved material crystallinity and UC emission. There is a significant host domain crystallinity increase depending on the annealing condition (i) to condition(ii). All of the XRD results showed that different concentrations of co-doping were observed in different accomplished XRD patterns in hydrous and anhydrous phases.

2.5% Er^{3+}-5% Tm^{3+} co-doped K-LTO (i) and 20%Er^{3+}-2.5%Tm^{3+} co-doped K-LTO (ii) SEM images were given in Figures 20(a) and Figure 20(b), respectively. Figure 20(a) and 20(b) have different morphology which show their interlayer structure, clearly. 2.5%Er^{3+}-5%Tm^{3+} co-doped K-LTO includes small and nonuniform nanoparticles. SEM images showed that they have a more uniform form with an increase of annealing temperature because of the temperature difference between figure 20(a) (900-1100 ºC) and figure 20(b) (1000-1200 ºC).

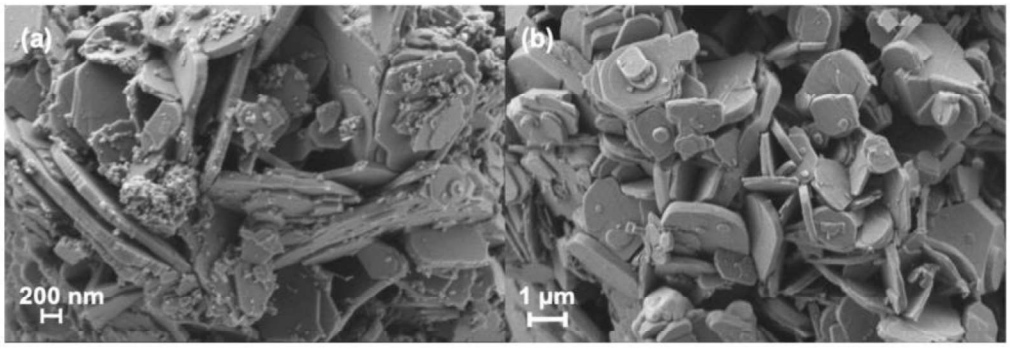

Figure 20. (a)K-LTO co-doped with 2.5% Er^{3+}-5% Tm^{3+} (i) and (b)K-LTO co-doped with 20% Er^{3+}-2.5% Tm^{3+} (ii) SEM images

Besides, layered perovskites having between 300 nm-2.5 µm lateral sizes were understood with SEM images given in Figure 20(b). Lateral size has to be higher and the thickness of layers smaller for the preparation of 2D nanosheets in their aspect ratio.

4.2. Spectral Characterization of Er^{3+}-Tm^{3+} Co-doped Layered Perovskites

The visible spectrum indicates blue color in 430-480 nm, green color in 480-560 nm, and red color in 620-700nm(Zwinkels and Canada, 2016). Related to the

increase of Er^{3+} ions at constant Tm^{3+} ions' concentration, the intensity goes from green to red for layered synthesized perovskites which is shown in the Commission International de L'Eclairage (CIE) chromaticity diagram in Figure 21. 20%Er^{3+}-2.5%Tm^{3+} co-doped K-LTO demonstrated an intense red color located in the CIE diagram. This is one of the aims for this thesis because of the nanofilm fabrication studies. Sağlam, (2020) reported that the Tm^{3+}/Yb^{3+} and Er^{3+}/Yb^{3+} co-doped K-LTO for the intense blue color and green color, respectively which were used for nanofilm fabrication. Due to UC emission results of layered perovskites, 20%Er^{3+}-2.5%Tm^{3+} co-doped K-LTO was used as the representative red color for RGB(Red-Green-Blue) upconverted nanofilms.

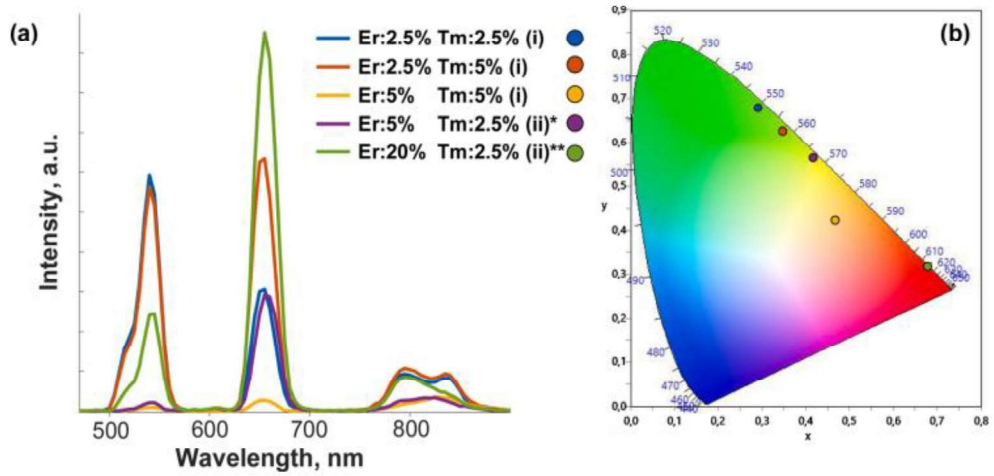

Figure 21. (a) K-LTO co-doped with Er^{3+}/Tm^{3+} UC emission under the 980 nm excitation (Laser power of 52.1mW/cm^2, *25.8mW/cm^2, **5.1 mW/cm^2), (b) Layered co-doped K-LTO perovskites (CIE) chromaticity Diagram

Increasing Er^{3+} concentration of synthesis indicates the reduction of intensity when the Tm^{3+} concentration is stabile for the red-green and NIR emission. 2.5%Er^{3+}-5%Tm^{3+} co-doped K-LTO has UC emission at 540 nm (green), 655 nm (red), and 795 nm (NIR) according to 980 nm power excitation. Laser power changes affected the UC emission and, UC emission was increased from lower to higher laser powers given in Figure 22(a). The UC mechanism process is related to the electron population and a minimum number of photons (n). The minimum number of photons(n) was calculated 2.1 for green, 1.7 for red emission, and 1.3 for NIR emission and they represent two-photon processes given in figure 22(b).

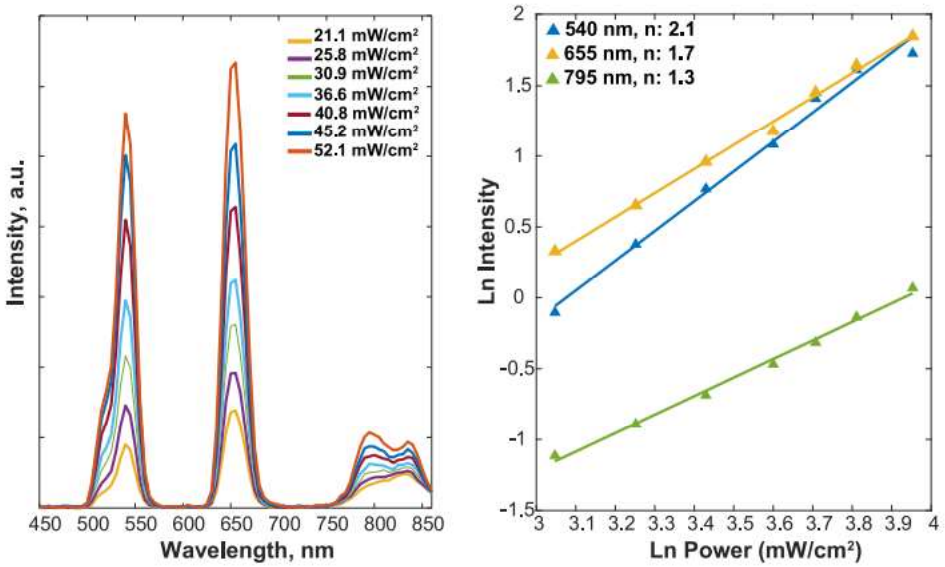

Figure 22. K-LTO co-doped with 2.5%Er^{3+}-5%Tm^{3+} for (a) Intensity relation of UC emission due to different laser power (b) Visible and NIR emission intensity log-log plot with excitation power

The schematic level diagram for Er^{3+} and Tm^{3+} was shown in figure 23. In the literature, green emissions are defined as $^4S_{3/2} \rightarrow {}^4I_{15/2}$ and $^2H_{11/2} \rightarrow {}^4I_{15/2}$, besides that red emissions are defined as $^4F_{9/2} \rightarrow {}^4I_{15/2}$ with the Er^{3+} transition. (Chai et al., 2012). Ground-state absorption (GSA) is the process related to electrons excitation that the Er^{3+} electrons transmission was observed from $^4I_{15/2}$ orbital level to $^4I_{11/2}$.

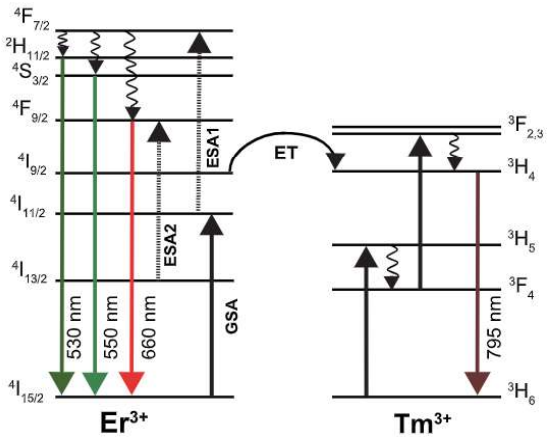

Figure 23. Schematic energy level diagram of Er^{3+} – Tm^{3+} co-doped K-LTO and oxide nanosheets as a possible upconversion mechanism based on two photons

Two-photon processes occurred by energy state absorption (ESA1) after the GSA process ($^4I_{11/2} \rightarrow {}^4F_{7/2}$). There are two possible ways for the intense red emission($^4F_{9/2} \rightarrow {}^4I_{15/2}$), firstly, non-radiative decay occurs from $^4F_{7/2}$ level to $^4F_{9/2\ after}$ the ESA1 process and secondly, ESA2 process consists of from 4 $I_{13/2}$ to $^4F_{9/2.}$ On the other hand, from Er^{3+} to Tm^{3+} can be energy transfer (ET) from $^4I_{9/2}$ to the $^3H_4$ level.

4.3. Ion Exchange for Layered Perovskites

The protonation step has an important place for the synthesis of two-dimensional nanosheets. Because protonation is the last process before exfoliating the layered materials. This step takes place for the exchange of potassium ions(K^+) and hydrogen(H^+) ions. The ion exchange for layered perovskites was optimized by applying different HCl acid concentrations between 0.5M and 3M. The XRD patterns of ion exchange associated with their layered forms are shown in Figure 24.

Layered materials XRD patterns were used which are Tm^{3+}-Yb^{3+} and Er^{3+}-Yb^{3+} co-doped K-LTO reported by Sağlam(2020). Tm^{3+}-Er^{3+} co-doped K-LTO XRD patterns were also published by us during this thesis study (Gunay et al. 2021). Different protonation concentrations were tried according to Tm^{3+}-Yb^{3+} co-doped K-LTO. Also, Tm^{3+}-Er^{3+} and Er^{3+}-Yb^{3+} co-doped K-LTO layered perovskites were protonated with 0.5M HCl, after the understanding of which acid molarity can be useful.

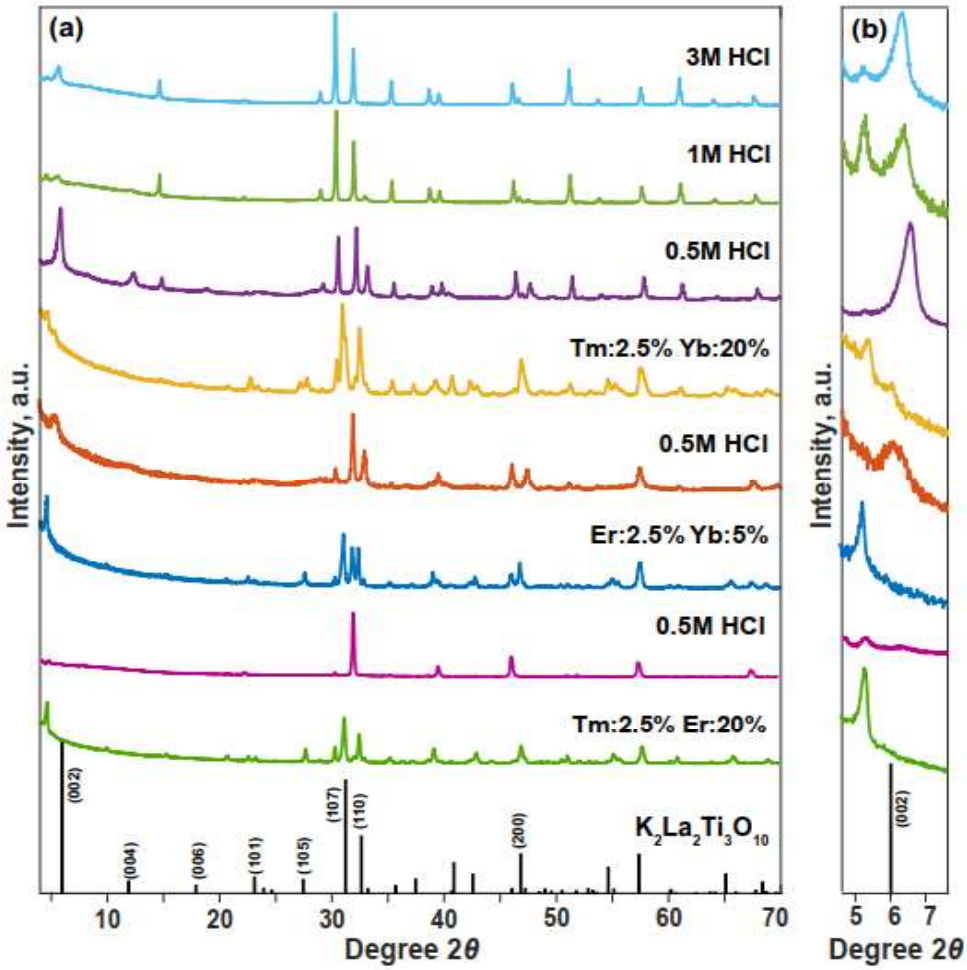

Figure 24. (a) Er^{3+}-Tm^{3+}, Er^{3+}-Yb^{3+} and Tm^{3+}-Yb^{3+} co-doped K-LTO and their Ion exchanged samples' XRD patterns (b) 5-7° region magnification of XRD patterns

Regarding XRD patterns, the protonated samples having a (001) diffraction peak was shifted to the higher angles which are given in figure 24(b) and this showed that the protonation was completed. Furthermore, the higher molarity of acids in the hydrous phase was shown to intercalate the water ions into the co-doped H-LTO synthesis in the XRD patterns. It was understood that the proton exchange with 0.5M acid was more successful when the (001) peaks were examined. Morphological changes of Tm^{3+}-Yb^{3+} co-doped K-LTO and its protonated samples were examined with the SEM images that are given in figure 25.

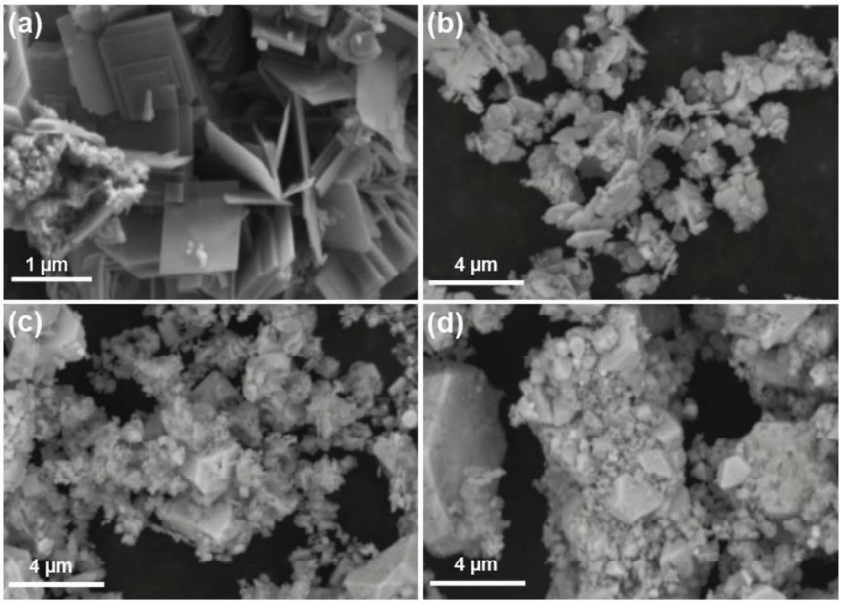

Figure 25. SEM images of (a) 2.5%Tm^{3+}-20%Yb^{3+} co-doped K-LTO layered perovskites, (b) 0.5M HCl, (c) 1M HCl, and (d) 3M HCl aqueous protonation

SEM images showed that the protonation of 1M and 3M acid concentration damaged the interlayer form of layered perovskites and the flake sizes had smaller morphology like comminuted shown in Figure 25(c) and Figure 25(d), respectively. On the other hand, 0.5M HCl aqueous protonation having between 500 nm and 2 µm lateral sizes was shown in figure 25(b). Ion exchange study showed that 0.5M HCl can be a better option for protonation of this type of layered perovskites.

4.4. The Structure and Morphology of 2D Perovskite Nanosheets

Tm^{3+}-Er^{3+}, Er^{3+}-Yb^{3+}, and Tm^{3+}-Yb^{3+} co-doped H-LTO protonated perovskites were exfoliated using the TBAOH solution. The nanosheets were coated onto the mica substrates by dripping the solution on the substrate. In addition, the Tyndall effect in aqueous form was observed for each nanosheet solution with the laser light in the dark area. This is related to colloidal forms of nanosheets having less thickness. For this reason, nanosheets can be spread to every level of water. If the nanosheet solution includes nanoparticles that are heavier than nanosheets, these nanoparticles can go down and that can be sedimentation. At this point, the supernatant from the nanosheet solution was separated into the new tubes and the pellet in the first tube was not used. Figure 26 shows the AFM images of three different co-doped nanosheets in order of

LTO co-doped with 2.5%Er^{3+}-5%Yb^{3+} (a), 2.5%Tm^{3+}-20%Yb^{3+} (b) and 2.5%Tm^{3+}-20%Er^{3+} (c).

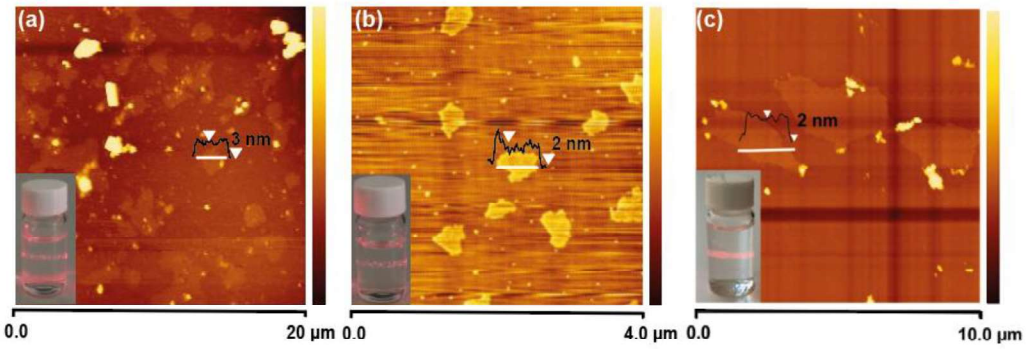

Figure 26. AFM images including height profile of nanosheets and Tyndall effects for (a) 2.5%Er^{3+}-5%Yb^{3+}, (b) 2.5%Tm^{3+}-20%Yb^{3+} and (c) 2.5%Tm^{3+}-20%Er^{3+}

AFM images showed 2D nanosheets having 2-3 nm thickness and their lateral sizes were observed from 500 nm to 2 um. On the other side, the images showed nonhomogeneous nanosheets because the nanosheet solution includes smaller and larger particles and this can affect the coating of substrate. The Tyndall effect is the colloidal scattering that shows into the AFM images. UC emission was analyzed for the nanosheet solutions as given in Figure 27.

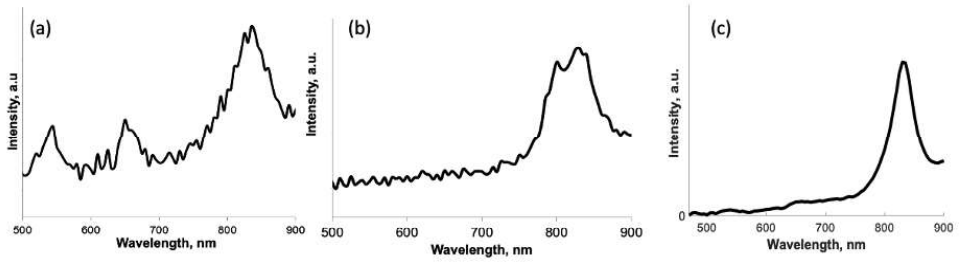

Figure 27. UC emission of Nanosheet solutions (a) Er^{3+}-Yb^{3+}, (b)Tm^{3+}-Yb^{3+} and (c) Tm^{3+}-Er^{3+} co-doped LTO respectively

For the Er^{3+}-Yb^{3+} co-doped LTO, there are two peaks in the range of visible emission at 540 nm($^2H_{11/2}$,$^4S_{3/2}$→$^4I_{15/2}$), and 660 nm($^4F_{9/2}$→$^4I_{15/2}$). There are intense peaks at the near-infrared emission (NIR). Although Tm^{3+}-Yb^{3+} and Tm^{3+}-Er^{3+} powder forms showed intense blue and red emission respectively, their colloidal forms did not show emission in the visible region.

In contrast, 2D nanosheets were analyzed in liquid solution. Because of the water diffraction difference, it might be refraction in the nanosheet solution. For this reason, peaks also may have a weak intensity.

4.5. Characterization of Layer-by-layer Films

For the preparation of layer-by-layer films, absorptions of nanosheets were observed with the sequence of 10 times. For this reason, 2.5%Er^{3+}-5%Yb^{3+} co-doped LTO nanosheets were coated on the ITO/glass substrates. When the coating number increased, absorption intensity increased in parallel with it shown in the region of 250-350 nm. The absorbance changed the absorbance related to the number of coatings according to 3, 5 and 10 layers is given Figure 28. On the other hand, PEI and PDDA polycations do not affect the absorbance intensity (T. Sasaki et al., 2000).

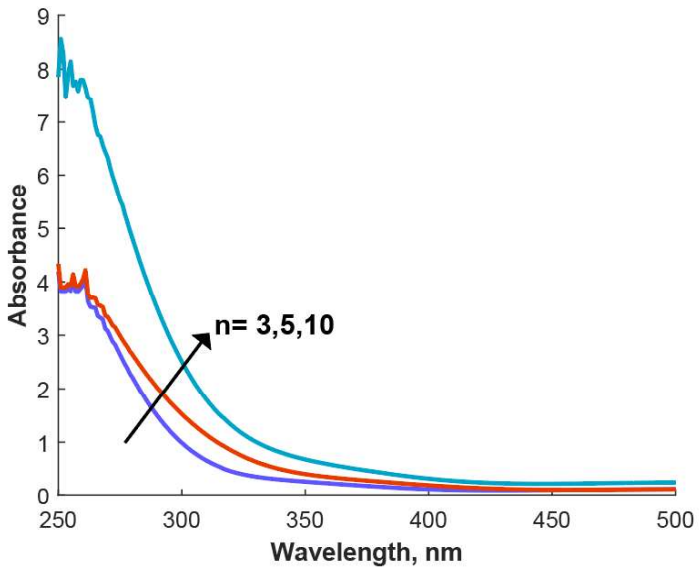

Figure 28. Layer-by-layer films UV-vis absorbance according to coating of nanosheets co-doped with 2.5%Er^{3+}-5%Yb^{3+}

The energy diagrams between Tm^{3+}, Er^{3+} and Yb^{3+} ions are shown in Figure 29.

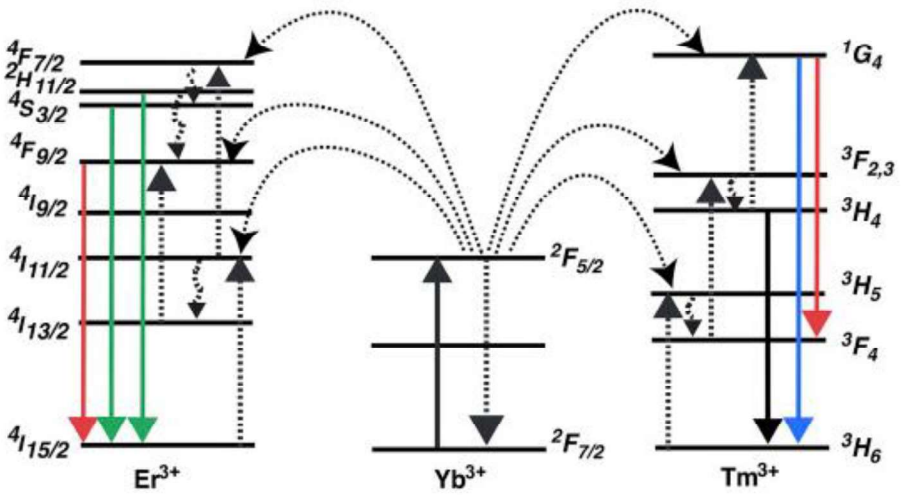

Figure 29. Energy level diagrams Yb^{3+}-Er^{3+} and Yb^{3+}-Tm^{3+} as the sensitizer/activator pairs (Source: Sağlam,2020)

Non-radiative relaxation of Yb^{3+} ions goes from $^2F_{5/2}$ to $^2F_{7/2}$ and the energy transition occurs from $^2F_{5/2}$ to $^4I_{11/2}$, $_4F_{9/2}$ and $_4F_{7/2\ for}$ the Er^{3+} states. The radiative decay of $^4S_{3/2}$ from $^2H_{11/2}$ causes the green emission of Er^{3+} ions. Two-photon processes are accomplishable for the green luminescence of Yb^{3+}-Er^{3+}(sensitizer-activator) from $^2H_{11/2}$ and $^4S_{3/2}$ to $^4I_{15/2}$. For the red fluorescence two-photon processes are possible, one of them $^4F_{9/2}$ to $^4I_{15/2}$ in Er^{3+} ion (Yb^{3+} sensitizer) and another photon process is from $^1G_4$ to $^3F_4$ in Tm^{3+} ion as an activator (Yb^{3+} sensitizer). From Yb^{3+} to Er^{3+} energy transfer for the red emission goes to $^4I_{11/2}$ and then multiphonon relaxation occurs to $^4I_{13/2}$. After that, nonradiative energy transfer from $^4I_{13/2}$ to $^4F_{9/2}$ induces red emission getting to $^4I_{15/2}$. Besides, there are two multiphonon relaxation by energy transition process from $^2F_{5/2}$ of Yb^{3+} ion related to red emission in the Er^{3+} ion which is from $^4F_{7/2}$ to $^2H_{11/2}$ and from $^2H_{11/2}$ to $^4F_{9/2}$. For the blue emission, the energy transition process from $^2F_{5/2}$ of Yb^{3+} ions can be transmitted directly $^1G_4$, $^3F_{2,3}$ or $^3H_5$. Blue emission occurs from $^1G_4$ to $^3H_6$. With the multiphonon relaxation from $^3F_{2,3}$ to $^3H_4$ affects nonradiative energy transfer to $^1G_4$ and indirectly blue luminescence can occur (Sağlam,2020).

The deposition of nanosheets with layer-by-layer assembly was completed with PDDA(3min)/nanosheet solution (15 min) dipping procedure. The nanosheets including all co-doping concentrations were coated on the quartz substrate to do multilayer 20 sequence film which is shown in Figure 30. Although the 20 sequence

films exhibited weak emissions, when the nanosheets were coated as films, they outperformed the emissions of nanosheet solutions. 2.5%Tm^{3+}-20%Er^{3+} co-doped film showed the peak having a lower intensity at 530 nm and 600 nm.

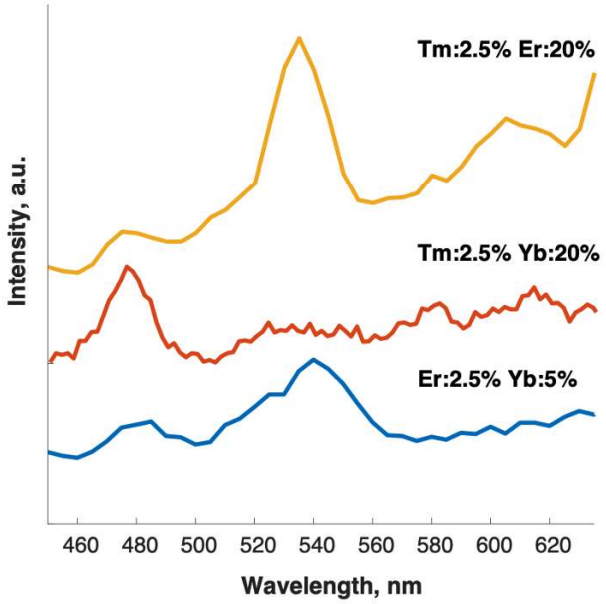

Figure 30. UC emission spectra of layer-by-layer films having 20 layers

On the other hand, 2.5%Tm^{3+}-20%Yb^{3+} co-doped films showed the weak blue emission region at 480 nm in visible light by transmission from $^1G_4$ to $^3H_6$. 2.5%Er^{3+}-5%Yb^{3+} co-doped nanosheets also intense the peak at 540 nm (the range of green region) in visible light. The transmission from Yb^{3+} to Er^{3+} can occur with two-photon processes from $^2H_{11/2}$ and $^4S_{3/2}$ to $^4I_{15/2}$.

During the film deposition process, it is aimed to coat the nanosheets homogeneously on the surface of the ITO/glass substrate by the layer-by-layer method. In this context, the layer-by-layer prepared film has been examined which is the AFM image shown in Figure 31. It was completed that the film coating homogeneously prepared 20 layers with 2.5% Tm^{3+}-20% Yb^{3+} co-doped nanosheets.

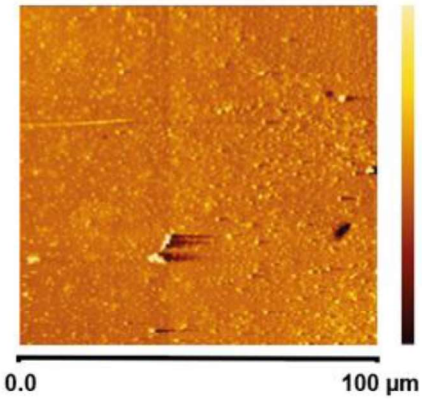

Figure 31. AFM image of film prepared 20 times with 2.5%Tm^{3+}-20%Yb^{3+} co-doped nanosheets

Nanosheets were deposited onto the ITO/glass substrates 30 layers using 2.5%Er^{3+}-5%Yb^{3+} co-doped nanosheets and 60 layers using 2.5%Er^{3+}-5%Yb^{3+}, 2.5%Tm^{3+}-20%Er^{3+} and 2.5%Tm^{3+}-20%Yb^{3+} co-doped nanosheets 20 times, respectively. The powder Er^{3+}-Yb^{3+} co-doped K-LTO, 30 layers and 60 layers Er^{3+}-Yb^{3+} co-doped films were shown in Figure 32.

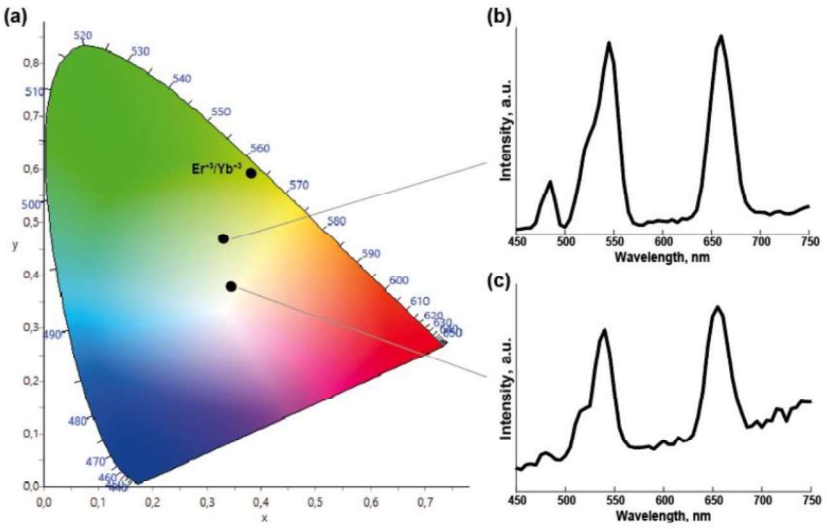

Figure 32. (a) 2.5%Er^{3+}-5%Yb^{3+} co-doped K-LTO and LTO films CIE diagram, (b) 30 layers nanosheet coatings as a layer-by-layer films and (c) 60 layers coating with red, blue and green region of nanosheets

The powder form of layered 2.5%Er^{3+}-5%Yb^{3+} co-doped perovskites showed the green color with its UC intensity results in the CIE diagram. Its nanosheet forms layer-by-layer coating showed the green emission with 30 sequences. On the other hand, green-blue-red color combinations show white color due to their reflection. In Figure 31(c), upconverting nanofilms were prepared as 20 layers Er^{3+}-Yb^{3+} co-doped nanosheets, 20 layers Tm^{3+}-Er^{3+} co-doped nanosheets and 20 layers Tm^{3+}-Yb^{3+} co-doped nanosheets. As a result, its CIE diagrams using UC emissions represented the white luminescence. In addition, UC emission was excited intensely at 540 nm($^4S_{3/2}\rightarrow{}^4I_{15/2}$ transmission) in the green visible region and 655 nm ($^4F_{9/2}\rightarrow{}^4I_{15/2}$ transmission) in the red visible region for 30 sequences of Er^{3+}-Yb^{3+} films and 60 sequences of combinated films.

The 30 sequences coated Yb^{3+}-Er^{3+} co-doped LTO were analyzed using a 980 nm NIR laser diode. From 16.78 mW/cm^2 to 52.1 mW/cm^2 laser powers were applied to the nanofilm coating and UC emission was shown in Figure 33.

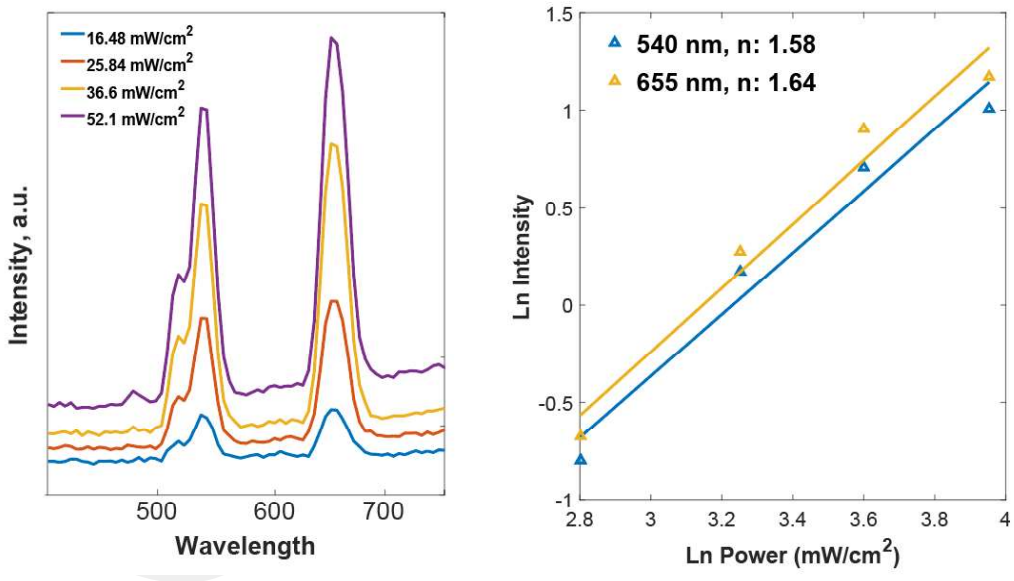

Figure 33. (a) UC emission intensity of 2.5%Yb^{3+}-5%Er^{3+} co-doped nanofilm coating (b) Visible and NIR emission intensity log-log plot with excitation power

The energy transfer from Yb^{3+} to Er^{3+} transmitted the photons from $^4S_{3/2}$ and $^2H_{11/2}$ to $^4I_{15/2}$ in the green region and from $^4F_{9/2}$ to $^4I_{15/2}$ in the red region. The films were analyzed from lower to higher laser powers. There was a significant increase especially at 540 nm and 655 nm in the visible region. The number of photons (n) was calculated as 1.58 at 540 nm and 1.64 at 655 nm. Therefore, two-photon emission processes consisted of the UC mechanism.

4.6. Cytotoxicity Analysis

Cytotoxicity analysis was carried out with the human HEK 293 kidney cell line and human HepG2 hepatocellular carcinoma cancer cell line. Their cell viability was analyzed with MTT assay and live-dead discrimination using the different concentrations of powder and nanosheet manipulations. The powder form of non-doped K-LTO and Tm^{3+}-Er^{3+} co-doped K-LTO were tried for the cell lines at 0, 10, 20, 50 and 100 µg/ml concentrations are given in Table 7. The Er^{3+}-Tm^{3+} co-doped K-LTO perovskites were toxic for HEK 293 cells when compared to other powders and only 10 ug/ml powder concentration affected for HEK 293 cells. Also, HEK 293 cells were affected by K-LTO powder perovskites whose viability was 62% in 100 µg/ml concentration. On the other hand, HepG2 cancer cells viability was higher (85.5%) at the concentration of 100 µg/ml Er^{3+}-Tm^{3+} co-doped K-LTO powders.

Table 5. HEK 293 and HepG2 cells cytotoxicity using powder form K-LTO and Tm^{3+}-Er^{3+} co-doped K-LTO

Conc. (ug/ml)	K-LTO (HEK 293)	K-LTO (HepG2)	Er^{3+}-Tm^{3+} co-doped K-LTO (HEK 293)	Er^{3+}-Tm^{3+} co-doped K-LTO (HepG2)
0	100	100	100	100
10	86.7	93.2	71.8	96.3
20	80.5	85.7	66.6	95.9
50	73.1	81.1	61.7	91.9
100	62	76.6	45.7	85.5

The nanosheet form of non-doped nanosheets and Tm^{3+}-Er^{3+} co-doped nanosheets were studied for the cell lines at the same concentrations given in Table 8. There was a difference between the powder form of Er^{3+}-Tm^{3+} co-doped K-LTO and LTO nanosheets for the HEK 293 cell line. Besides that, non-doped nanosheets affected the HepG2 cancer cells more than the non-doped K-LTO powder.

Table 6. HEK 293 and HepG2 cells cytotoxicity using nanosheet form LTO and Tm^{3+}-Er^{3+} co-doped LTO

Conc. (ug/ml)	LTO (HEK 293)	LTO (HepG2)	Er^{3+}/Tm^{3+} co-doped LTO (HEK 293)	Er^{3+}/Tm^{3+} co-doped LTO (HepG2)
0	100	100	100	100
10	88.8	89.2	81.3	94.5
20	85.4	85.6	78.9	90.7
50	81.3	69.8	75.9	86.1
100	63.2	65	73.6	83.6

HepG2, which is a cancer cell line, was less affected by the nanosheets and powder forms when compared with the HEK 293 normal cell line. However, toxicity was increased in high concentrations for all cell lines. In Figure 34, cell viability depends on the powder and nanosheet form of concentrations were shown.

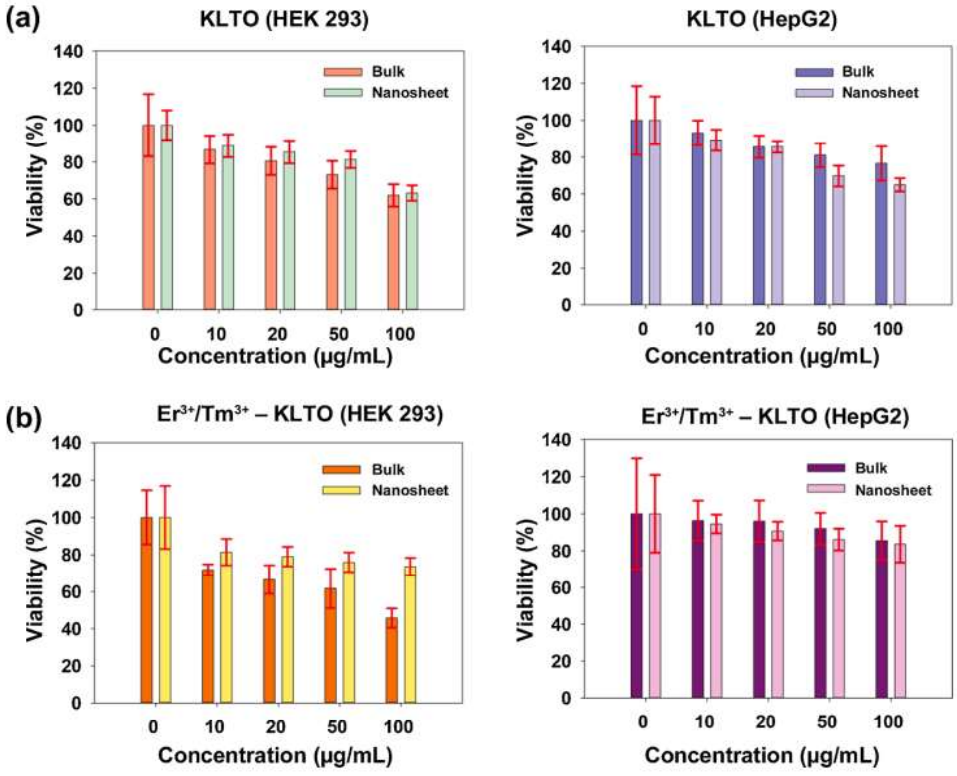

Figure 34. Cytotoxicity for HEK 293 and HepG2 of (a) non-doped K-LTO perovskite powders and nanosheets (b) Tm^{3+}-Er^{3+} co-doped K-LTO perovskite powders and nanosheets. Standard deviation (SD) showed with error bars.

Nanosheet form can be less toxic than a bulk form of layered perovskites for the HEK 293 cell viability. The bulk of K-LTO co-doped with Er^{3+}-Tm^{3+} showed high cytotoxicity to HEK 293 when compared to non-doped K-LTO. It can be related to the fact that Er^{3+}-Tm^{3+} are classified as heavy REMs (Roncati et al., 2018). HepG2 was not affected by the K-LTO co-doped with Er^{3+}-Tm^{3+}. However, in the literature, HepG2 hepatoma cells have been demonstrated to have high sensitivity compared to HEK 293 kidney cells for different heavy metals of cadmium (Cd) (Lawal and Ellis, 2010). Also, the increase of lanthanum concentration can be toxic for the cells (Kale et al., 2006). Nanosheet form of LTO showed less viability when comparing the LTO co-doped with Er^{3+}-Tm^{3+}. In Figure 35, visualization of cell viability was shown using light microscope and fluorescent microscope.

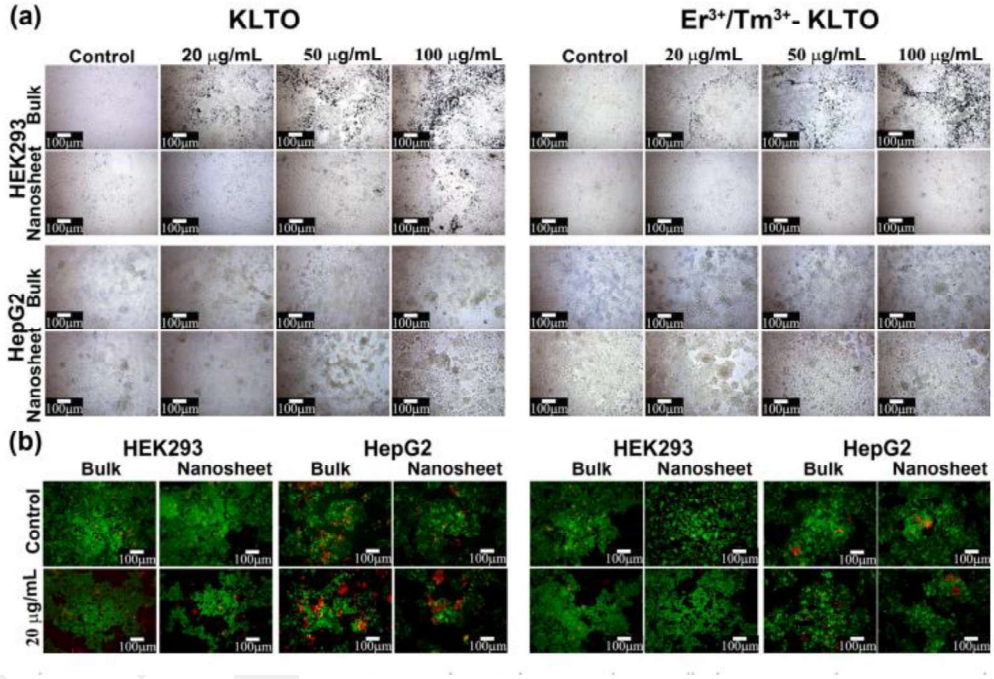

Figure 35. (a) Euromex Oxion Inverso light microscope images after 48 hours (b) Olympus 1X71 Fluorescent microscope images (green and red represent live and dead cells respectively) All images have a 100 um scale bar(10X magnification).

Cells lost their original shape after 50 μg/ml, all forms of nanomaterials addition and cell adhesion were affected negatively. In order to detect live and dead cells visually, the Calcein/PI assay was performed in each material concentration at 20 μg/ml. Non-fluorescent Calcein-AM can be converted by intracellular esterases to green fluorescent Calcein-AM in the live cells. Dead cells can be affected by PI

because PI directly enters into the dead cells and produces red luminescence. The Fluorescence microscope images showed that only K-LTO powders and nanosheets at 20 μg/ml were observed as apparent red luminescent for HepG2 dead cells.

CHAPTER 5: CONCLUSION

In this thesis, upconverted nanofilm coatings were studied for multifunctional device fabrication. Lanthanide doped RP-type perovskites and their 2D nanosheet form were analyzed for biocompatibility of the cells. In this regard, RP-type $K_2Ln_2Ti_3O_{10}$ layered perovskites were co-doped with lanthanides to have upconversion properties. Tm^{3+}-Er^{3+} co-doped K-LTO was synthesized with different concentrations of lanthanides. After the XRD patterns and UC emission of the layered materials were analyzed, 2.5%Tm^{3+}-20%Er^{3+} co-doped K-LTO was selected for the film fabrication because of its intense UC emission in the red region. In addition, the lateral size of the 2.5%Tm^{3+}-20%Er^{3+} co-doped K-LTO was within the range of 500 nm to 3 μm. A larger lateral area of nanosheets can be produced from layered materials having larger lateral sizes. 2.5%Er^{3+}-5%Yb^{3+} and 2.5%Tm^{3+}-20%Yb^{3+} co-doped K-LTO perovskites were also selected for green and blue emissions in the visible region, respectively. The results showed that the excitation for Er^{3+}-Tm^{3+}co-doped K-LTO perovskites occurred green emission transitions of $^2H_{11/2,}$ $^4S_{3/2}\rightarrow{}^4I_{15/2}$ (530-550 nm) and red emission transition of $^4F_{9/2}\rightarrow{}^4I_{15/2}$ (660 nm) in the Er^{3+} ion. The exchange of lanthanide ions with hydrogen atoms in the A region of the layered perovskites was determined according to the XRD analysis. As a result of protonation, (002), (004), (006) Bragg Miller indices were shifted towards higher 2 (theta) angles. Different acid concentrations were performed for protonation and except for 0.5M acid concentration, the crystal lattice forms were changed. The lateral size of the layered material before protonation was found as 300 nm to 2.5 μm due to the SEM analysis. After the protonation, lateral sizes of protonated materials were determined to be 2 μm. The protonated materials interacted with the $TBAOH^-$ solution for the exfoliation process which yielded a nanosheet solution. The thickness of the nanosheets was determined by AFM analysis as 2-3 nm thickness with a 500nm-1μm lateral size. When the nanosheet solutions were excited with a laser source at a wavelength of 980 nm, only Er^{3+}-Yb^{3+} co-doped nanosheet solutions showed two peaks in the visible region. On the other hand, 20 sequences of Er^{3+}-Yb^{3+}, Tm^{3+}-Yb^{3+} and Tm^{3+}-Er^{3+} co-doped films showed the emissions in the RGB visible region. When the nanofilm coating sequences from 3 to 10 were examined, their absorbances increased in the range of 250-350 nm for the dipping procedure of 20 min nanosheet solution / 20 min PDDA. Moreover, the nanofilms of 30 layers using Er^{3+}-Yb^{3+} and 60 layers using three

nanosheet combinations were produced. The films (30-60 layers) exhibited intense green $^4S_{3/2} \rightarrow {}^4I_{15/2}$ and red $^4F_{9/2} \rightarrow {}^4I_{15/2}$ transmissions. The 60-layer films including three nanosheet combinations were observed in the white color located in the CIE diagram. Two-photon emissions occurred for the 30 layers coated films because the scope of the UC emissions due to laser powers were calculated as 1.58(540 nm) and 1.64 (655 nm). Nanoparticle concentrations were applied to the HEK 293 and HepG2 cells from 10 to 100 µg/ml with control groups. After 50 µg/ml, the cell morphology was changed and cell adhesion was negatively affected. Nevertheless, Tm3+-Er3+ co-doped K-LTO was 45.7% toxic for HEK 293 cell lines, Tm^{3+}-Er^{3+} co-doped nanosheet material showed less toxicity (73.6%) for HEK 293 cell lines. The toxicity of nanosheets and bulk materials showed that although 100 µg/ml reduced cell viability, it was not very toxic because generally cell viability was above 60%.

REFERENCES

Allen, M. R., Thibert, A., Sabio, E. M., Browning, N. D., Larsen, D. S., and Osterloh, F. E. (2010) *Evolution of physical and photocatalytic properties in the layered titanates A2Ti4O9 (A = K, H) and in nanosheets derived by chemical exfoliation*. Chemistry of Materials, 22(3), pp. 1220–1228.

Allison, D. P., Mortensen, N. P., Sullivan, C. J., and Doktycz, M. J. (2010) *Atomic force microscopy of biological samples.* Wiley Interdisciplinary Reviews: Nanomedicine and Nanobiotechnology, 2(6), pp. 618-634.

Ansari, A. A., Siddiqui, M. A., Khan, A., Ahmad, N., and Al-Khedhairy, A. A. (2020) *Synthesis, optical properties and toxic potentiality of photoluminescent lanthanum oxide nanospheres.* Colloids and Surfaces A: Physicochemical and Engineering Aspects, 607, 125511 Available at : https://www.sciencedirect.com/science/article/pii/S0927775720311043 (Accessed: 1 June 2021).

Assirey, E. A. R. (2019). *Perovskite synthesis, properties and their related biochemical and industrial application.* Saudi Pharmaceutical Journal, 27(6), pp. 817–829.

Atta, N. F., Galal, A., and El-Ads, E. H. (2016). *Perovskite Nanomaterials – Synthesis, Characterization, and Applications.* Perovskite Materials- Synthesis, Characterisation, Properties, and Applications, pp. 107-151.

Azadmanjiri, J., Berndt, C. C., Wang, J., Kapoor, A., and Srivastava, V. K. (2016) *Nanolaminated composite materials: Structure, interface role and applications.* RSC Advances, 6(111), pp. 109361–109385.

Bergman, L., and McHale, J. L. (2011) *Handbook of luminescent semiconductor materials.*CRC Press, First Edition

Bhalla, A. S., Guo, R., and Roy, R. (2000). *The perovskite structure - A review of its role in ceramic science and technology*. Materials Research Innovations, 4(1), pp. 3–26.

B Bramowicz, M., Kulesza, S., and Rychlik, K. (2012) *A Comparison between Contact and Tapping AFM Mode in Surface Morphology Studies.* Technical Sciences, 15(2)

pp. 307-318.

Chai, G., Dong, G., Qiu, J., Zhang, Q., and Yang, Z. (2012) *2.7 μm emission from transparent Er 3+,Tm 3+ codoped yttrium aluminum garnet (Y 3Al 5O 12) nanocrystals-tellurate glass composites by novel comelting technology.* Journal of Physical Chemistry C, 116(37), pp. 19941–19950.

Chuang, Y. (2016). *Encyclopedia of Color Science and Technology.*Springer Reference, pp. 935-937.

Dierickx, B., Dupont, B., Defernez, A., and Ahmed, N. (2011). *Color X-ray photon counting image sensing.* In IISW, Hakodate Japan, 1. Available at: https://caeleste.be/wp-content/uploads/2018/03/2011-iisw-qx.pdf (Accessed: 1 June 2021).

Ding, J., Ming, J., Lu, D., Wu, W., Liu, M., Zhao, X., Li, C., Yang, M., and Fang, P. (2017) S*tudy of the enhanced visible-light-sensitive photocatalytic activity of Cr2O3-loaded titanate nanosheets for Cr(VI) degradation and H2 generation.* Catalysis Science and Technology, *7*(11), pp. 2283–2297.

Domen, K., Yoshimura, J., Sekine, T., Kondo, J., Tanaka, A., Maruya, K., and Onishi, T. (1993). *A novel series of photocatalysts with an ion-exchangeable layered structure of niobate.* Studies in Surface Science and Catalysis, 75(C), pp. 2159–2162.

Fu, L., Yan, Z., Zhao, Q., and Yang, H. (2018). *Novel 2D Nanosheets with Potential Applications in Heavy Metal Purification: A Review.* Advanced Materials Interfaces, 5(23), pp. 22–25.

Ge, Y. Y., Zhao, Y. J., Yuan, X. Y., Sun, S. Y., Zhao, Y. Z., and Zhou, H. P. (2016). *Synthesis of Er3+-doped perovskite nanorods with outstanding UC PL behavior.* RSC Advances, 6(71), pp. 67353–67360.

Geim, A. K. (2012). *Graphene prehistory*. Physica Scripta, 2012(T146), pp. 014003.

Avaliable at: https://iopscience.iop.org/article/10.1088/0031-8949/2012/T146/014003/meta (Accessed: 2 June 2021)

Gunay, B., Sarıyar, E., Unal, U., Firtina Karagonlar, Z., and Sağlam, Ö. (2021). *Upconversion properties of Tm3+-Er3+ co-doped layered perovskites and in-vitro cytotoxicity of their exfoliated nanomaterials*. Colloids and Surfaces A:

Physicochemical and Engineering Aspects, 612, 126003. Available at: https://www.sciencedirect.com/science/article/pii/S092777572031596X (Accessed: 5 June 2021).

Hines, R. I., Allan, N. L., and Flavell, W. R. (1996). *Oxidation catalysts: A comparative simulation study of the lattice, defect and surface structure of the stannates ASnO3 (A = Ca, Sr and Ba) and SnO2.* Journal of the Chemical Society - Faraday Transactions, 92(12), pp. 2057–2063.

Ida, S., Ogata, C., Eguchi, M., Youngblood, W. J., Mallouk, T. E., and Matsumoto, Y. (2008). *Photoluminescence of perovskite nanosheets prepared by exfoliation of layered oxides, K2Ln2Ti3O10, KLnNb2O7, and RbLnTa2O7 (Ln: lanthanide ion).* Journal of the American Chemical Society 130(22), pp. 7052-7059.

Inkson, B. J. (2016) *Scanning electron microscopy (SEM) and transmission electron microscopy (TEM) for materials characterization.* Materials characterization using nondestructive evaluation (NDE) methods. Woodhead Publishing. pp. 17-43.

Kale, S. N., Arora, S., Bhayani, K. R., Paknikar, K. M., Jani, M., Wagh, U. V., Kulkarni, S. D., and Ogale, S. B. (2006). *Cerium doping and stoichiometry control for biomedical use of La0.7Sr0.3MnO3 nanoparticles: microwave absorption and cytotoxicity study.* Nanomedicine: Nanotechnology, Biology, and Medicine, 2(4), pp. 217–221.

Kim, W. J., Nyk, M., and Prasad, P. N. (2009). *Color-coded multilayer photopatterned microstructures using lanthanide (III) ion co-doped NaYF4 nanoparticles with upconversion luminescence for possible applications in security.* Nanotechnology, 20(18), 185301. Available at: https://iopscience.iop.org/article/10.1088/0957-4484/20/18/185301/meta (Accessed: 5 June 2021).

Kumar, S. B. R. D. (2011). *Photon avalanche upconversion and pump power studies in LaF 3 : Er 3 + / Yb 3 + phosphor*. Applied Physics B 104(4), pp. 1035–1041.

Lawal, A. O., and Ellis, E. (2010). *Differential sensitivity and responsiveness of three human cell lines HepG2, 1321N1 and HEK 293 to cadmium.* Journal of Toxicological Sciences, 35(4), pp. 465–478.

Li, P. P., Yan, Y., Zhang, H. T., Cui, S. he, Wang, C. H., Wei, W., Qian, H. G., Wang, J. C., and Zhang, Q. (2020). *Biological activities of siRNA-loaded lanthanum*

phosphate nanoparticles on colorectal cancer. Journal of Controlled Release, 328, pp. 45–58.

Liao, C., Li, Y., and Tjong, S. C. (2018). *Graphene nanomaterials: Synthesis, biocompatibility, and cytotoxicity.* International Journal of Molecular Sciences, 19(11), 3564. Available at: https://www.mdpi.com/1422-0067/19/11/3564 (Accessed: 6 June 2021).

Ma, R., and Sasaki, T. (2010). *Nanosheets of oxides and hydroxides: Ultimate 2D charge-bearing functional crystallites.* In Advanced Materials, 22(45), pp. 5082-5104.

Maver, U., Maver, T., Peršin, Z., Mozetič, M., Vesel, A., Gaberšček, M., and Stana Kleinschek, K. (2013) *Polymer characterization with the atomic force microscope.* Polymer science, 4, pp. 1200-1208.

Meruga, J. M., Baride, A., Cross, W., Kellar, J. J., and May, P. S. (2014). *Red-green-blue printing using luminescence-upconversion inks*. Journal of Materials Chemistry C, *2*(12), pp. 2221–2227.

Nag Bhargavi, G., and Khare, A. (2015). *Luminescence studies of perovskite structured titanates: A review.* Optics and Spectroscopy, 118(6), pp. 902–917.

Szuromi, P., and Grocholski, B., (2017) *Perovskites*, Natural and engineered. 358(6364), pp. 732–734.

Nogueira, D., Mitjans, M., Rolim, C., and Vinardell, M. (2014). *Mechanisms Underlying Cytotoxicity Induced by Engineered Nanomaterials: A Review of In Vitro Studies.* Nanomaterials, 4(2), pp. 454–484.

Ono, L. K., Juarez-Perez, E. J., and Qi, Y. (2017). *Progress on Perovskite Materials and Solar Cells with Mixed Cations and Halide Anions*. ACS Applied Materials and Interfaces, 9(36), pp. 30197–30246.

Osada, M., and Sasaki, T. (2009). *Exfoliated oxide nanosheets: New solution to nanoelectronics.* Journal of Materials Chemistry, 19(17), pp. 2503–2511.

Osada, M., and Sasaki, T. (2012). *Two-dimensional dielectric nanosheets: Novel nanoelectronics from nanocrystal building blocks.* Advanced Materials, 24(2), pp. 210-228.

Osada, M., and Sasaki, T. (2018). *Nanoarchitectonics in dielectric/ferroelectric layered perovskites: From bulk 3D systems to 2D nanosheets.* Dalton Transactions, 47(9), pp. 2841–2851.

Ovsyakin, V., and Feofilov, P. (1966). *Cooperative Sensitization of Luminescence in Crystals Activated with Rare Earth Ions.* In Soviet Journal of Experimental and Theoretical Physics Letters 4, 317. Available at: https://ui.adsabs.harvard.edu/abs/1966JETPL...4..317O/abstract (Accessed: 6 June 2021)

Pan, L. Y., Ding, Y. F., Yu, Z. L., Wan, Q., Liu, B., and Cai, M. Q. (2020). *Layer-dependent optoelectronic property for all-inorganic two-dimensional mixed halide perovskite Cs2PbI2Cl2 with a Ruddlesden-Popper structure.* Journal of Power Sources, 451, 227732. Available at: https://www.sciencedirect.com/science/article/pii/S0378775320300355 (Accessed: 6 June 2021).

Pazik, R., Ziecina, A., Poźniak, B., Malecka, M., Marciniak, L., and Wiglusz, R. J. (2016). *Up-conversion emission and in vitro cytotoxicity characterization of blue emitting, biocompatible SrTiO3 nanoparticles activated with Tm3+ and Yb3+ ions.* RSC Advances, 6(45), pp. 39469–39479.

Ramos, A. P., Cruz, M. A. E., Tovani, C. B., and Ciancaglini, P. (2017). *Biomedical applications of nanotechnology*. In Biophysical Reviews, 9(2), pp. 79-89.

Rodionov, I. A., Maksimova, E. A., Pozhidaev, A. Y., Kurnosenko, S. A., Silyukov, O. I., and Zvereva, I. A. (2019). *Layered Titanate H2Nd2Ti3O10 Intercalated With n-Butylamine: A New Highly Efficient Hybrid Photocatalyst for Hydrogen Production From Aqueous Solutions of Alcohols.* Frontiers in Chemistry 7, 863. Available at: https://www.frontiersin.org/articles/10.3389/fchem.2019.00863/full (Accessed: 6 June 2021)

Roncati, L., Gatti, A. M., Barbolini, G., Piscioli, F., Pusiol, T., and Maiorana, A. (2018). *In vivo uptake of rare earth metals by triple-negative breast cancer cells.* Pathology and Oncology Research, 24(1), pp. 161-165.

Sağlam, Ö. (2020). *Concentration based multicolor upconversion emission of lanthanides Co-doped Ruddlesden-Popper type layered perovskites.* Optical Materials,

109, 110294. Available at: https://www.sciencedirect.com/science/article/pii/S0925346720306352 (Accessed: 6 June 2021).

Sasaki, T., Ebina, Y., Tanaka, T., Harada, M., Watanabe, M., and Decher, G. (2001). *Layer-by-layer assembly of titania nanosheet/polycation composite films*. Chemistry of Materials, 13(12), pp. 4661–4667.

Sasaki, T., Ebina, Y., Watanabe, M., and Decher, G. (2000). *Multilayer ultrathin films of molecular titania nanosheets showing highly efficient UV-light absorption*. Chemical Communications, 21, pp. 2163–2164.

Sasaki, Takayoshi, Watanabe, M., Hashizume, H., Yamada, H., and Nakazawa, H. (1996). *Macromolecule-like aspects for a colloidal suspension of an exfoliated titanate. Pairwise association of nanosheets and dynamic reassembling process initiated from it*. Journal of the American Chemical Society, 118(35), pp. 8329–8335.

Schaak, R. E., and Mallouk, T. E. (2002). *Perovskites by design: A toolbox of solid-state reactions.* Chemistry of Materials, 14(4), pp. 1455–1471.

Shi, P., and Huang, Z. (2005). *Proteomic detection of changes in protein synthesis induced by lanthanum in BGC-823 human gastric cancer cells.* BioMetals, 18(1), pp. 89-95.

Silyukov, O. I., Kulish, L. D., Trofimova, D. V., Burovikhina, A. A., Chislov, M. V., Rodionov, I. A., Zhukov, Y. M., and Zvereva, I. A. (2018). *Formation of vanadium-containing nanostructures on the surface of protonated forms of layered perovskite-like titanates K2La2Ti3O10 and NaLaTiO4.* Journal of Solid State Chemistry, 259, pp. 28–34.

Su, L., Fan, X., Yin, T., Wang, H., Li, Y., Liu, F., Li, J., Zhang, H., and Xie, H. (2020). *Inorganic 2D Luminescent Materials: Structure, Luminescence Modulation, and Applications.* Advanced Optical Materials, *8*(1), pp. 1–40.

Su, X., Zheng, X., and Ni, J. (2009). *Lanthanum citrate induces anoikis of Hela cells.* Cancer Letters, 285(2), pp. 200–209.

Sugimoto, W., Yokoshima, K., Ohuchi, K., Murakami, Y., and Takasu, Y. (2006). *Fabrication of Thin-Film, Flexible, and Transparent Electrodes Composed of*

Ruthenic Acid Nanosheets by Electrophoretic Deposition and Application to Electrochemical Capacitors. Journal of The Electrochemical Society, *153*(2), A255. Available at: https://iopscience.iop.org/article/10.1149/1.2138570/meta (Accessed: 6 June 2021)

Sun, Z., Shu, D., Lv, C., Zhang, Q., He, C., and Tian, S. (2013). *Fabrication and supercapacitive behavior of tetramethylammonium ion-intercalated MnO2 prepared by an exfoliation and self-assembly process.* Journal of Alloys and Compounds, 569, pp. 136–143.

Khodabakhsh, M. (2018) *Synthesis and Optical Characterization of Aurivillius Layered Perovskites*. Submitted Doctoral Thesis, Koç University.

Tahara, S., Ichikawa, T., Kajiwara, G., and Sugahara, Y. (2007). *Reactivity of the Ruddlesden-Popper phase H2la 2Ti3O10 with organic compounds: Intercalation and grafting reactions.* Chemistry of Materials, 19(9), pp. 2352–2358.

Taniguchi, T., Murakami, T., Funatsu, A., Hatakeyama, K., Koinuma, M., and Matsumoto, Y. (2014). *Reversibly tunable upconversion luminescence by host-guest chemistry.* Inorganic Chemistry, *53*(17), pp. 9151–9155.

Thanh, T. D., Chuong, N. D., Hien, H. Van, Kshetri, T., Tuan, L. H., Kim, N. H., and Lee, J. H. (2018). *Recent advances in two-dimensional transition metal dichalcogenides-graphene heterostructured materials for electrochemical applications.* Progress in Materials Science, 96, pp. 51–85.

Tidrow, S. C. (2014). *Mapping comparison of goldschmidt's tolerance factor with perovskite structural conditions.* Ferroelectrics, 470(1), pp. 13–27.

Toda, K., Watanabe, J., and Sato, M. (1996). *Crystal structure determination of ion-exchangeable layered perovskite compounds, K2La2Ti3O10 and Li2La2Ti3O10.* Materials Research Bulletin, 31(11), pp. 1427–1435.

Tomczak, N., Eng, K., Goh, J., and Scientific, W. (2010). *Scanning probe microscopy.* World Scientific.

Tsang, M. K., Bai, G., and Hao, J. (2015). *Stimuli responsive upconversion luminescence nanomaterials and films for various applications.* Chemical Society Reviews, 44(6), pp. 1585–1607.

Tsukruk, V. V., and Singamaneni, S. (2012). *Scanning probe microscopy of soft matter: fundamentals and practices.* John Wiley and Sons.

Twentyman PR, and Luscombe M. (1987). A *study of some variables in a tetrazolium dye (MTT) based assay for cell growth and chemosensitivity*. British Journal of Cancer, 56(3), pp. 279–285.

Uppuluri, R., Sen Gupta, A., Rosas, A. S., and Mallouk, T. E. (2018). *Soft chemistry of ion-exchangeable layered metal oxides.* In Chemical Society Reviews, 47(7), pp. 2401-2430.

Urie, R., Ghosh, D., Ridha, I., and Rege, K. (2018). *Inorganic Nanomaterials for Soft Tissue Repair and Regeneration.* Annual Review of Biomedical Engineering, 20, pp. 353-374.

Uygur, B., Craig, G., Mason, M. D., and Ng, A. K. (2009). *Cytotoxicity and genotoxicity of silver nanomaterials.* Technical Proceedings of the 2009 NSTI Nanotechnology Conference and Expo, NSTI-Nanotech 2009, *2*, pp. 383–386.

Valeur, B., and Berberan-Santos, M. N. (2011). *A brief history of fluorescence and phosphorescence before the emergence of quantum theory*. Journal of Chemical Education, 88(6), pp.731–738.

Vendruscolo, V., Giordano, L., Constantino, V. R. L., and Rodrigues, L. C. V. (2020). *Yb3+/Er3+co-doped Dion-Jacobson niobium layered perovskites as NIR-To-green upconversion materials.* New Journal of Chemistry, 44(24), pp. 10165–10171.

Wang, C., Osada, M., Ebina, Y., Li, B. W., Akatsuka, K., Fukuda, K., Sugimoto, W., Ma, R., and Sasaki, T. (2014). *All-nanosheet ultrathin capacitors assembled layer-by-layer via solution-based processes.* ACS Nano, 8(3), pp. 2658–2666.

Wang, L., Cui, D., Ren, L., Zhou, J., Wang, F., Casillas, G., Xu, X., Peleckis, G., Hao, W., Ye, J., Dou, S. X., Jin, D., and Du, Y. (2019). *Boosting NIR-driven photocatalytic water splitting by constructing 2D/3D epitaxial heterostructures.* Journal of Materials Chemistry A, *7*(22), pp. 13629–13634.

Wu, J., Yang, J., Liu, Q., Wu, S., Ma, H., and Cai, Y. (2013). *Lanthanum induced primary neuronal apoptosis through mitochondrial dysfunction modulated by Ca2+ and Bcl-2 family.* Biological Trace Element Research, 152(1), pp. 125-134.

Xia, T., Kovochich, M., Liong, M., Zink, J. I., and Nel, A. E. (2008). *Cationic polystyrene nanosphere toxicity depends on cell-specific endocytic and mitochondrial injury pathways.* ACS Nano, *2*(1), pp. 85–96.

Xu, Z., Gao, Y., Huang, S., Ma, P. A., Lin, J., and Fang, J. (2011). *A luminescent and mesoporous core-shell structured Gd2O 3:Eu3+@nSiO2@mSiO2 nanocomposite as a drug carrier.* Dalton Transactions, 40(18), pp. 4846-4854.

Yamasue, K., Kobayashi, K., Yamada, H., Matsushige, K., and Hikihara, T. (2009). *Controlling chaos in dynamic-mode atomic force microscope*. Physics Letters A, *373*(35), pp. 3140–3144.

Yang, M., Xiang, G., Li, D., Zhang, Y., Xu, W., and Tao, L. (2016). *The insecticide spinosad induces DNA damage and apoptosis in HEK293 and HepG2 cells.* Mutation Research - Genetic Toxicology and Environmental Mutagenesis, 812, pp. 12–19.

Yu, L., Xiong, J., Guo, L., Miao, L., Liu, S., and Guo, F. (2015). *The effects of lanthanum chloride on proliferation and apoptosis of cervical cancer cells: Involvement of let-7a and miR-34a microRNAs.* BioMetals, 28(5), pp. 879–890.

Zhang, J., Li, Y., Hao, X., Zhang, Q., Yang, K., Li, L., Ma, L., Wang, S., and Li, X. (2012). *Recent Progress in Therapeutic and Diagnostic Applications of Lanthanides.* Mini-Reviews in Medicinal Chemistry, 11(8), pp. 678–694.

Zheng, K., Loh, K. Y., Wang, Y., Chen, Q., Fan, J., Jung, T., Nam, S. H., Suh, Y. D., and Liu, X. (2019). *Recent advances in upconversion nanocrystals: Expanding the kaleidoscopic toolbox for emerging applications.* Nano Today, 29, 100797. Available at: https://www.sciencedirect.com/science/article/pii/S1748013219302555 (Accessed: 6 June 2021)

Zhou, B., Shi, B., Jin, D., and Liu, X. (2015). *Controlling upconversion nanocrystals for emerging applications.* Nature Nanotechnology, *10*(11), pp. 924–936.

Zhu, Y., Peng, L., Fang, Z., Yan, C., Zhang, X., and Yu, G. (2018). *Structural Engineering of 2D Nanomaterials for Energy Storage and Catalysis.* Advanced Materials, 30(15), pp. 1–19.

Zwinkels, J. (2015). *Light, electromagnetic spectrum.* Encyclopedia of Color Science and Technology, pp. 1-8.